Università Milano Bicocca

Adsorption and Scattering Phenomena in Materials Science

Filippo Carone Fabiani

A dissertation submitted in partial
fulfilment of the requirements
for the degree of Doctor of Philosophy

Department of Materials Science

March 2014

"But the secret of intellectual excellence is the spirit of criticism; it is intellectual independence. And this leads to difficulties which must prove insurmountable for any kind of authoritarianism. The authoritarian will in general select those who obey, who believe, who respond to his influence. But in doing so, he is bound to select mediocrities. For he excludes those who revolt, who doubt, who dare to resist his influence. Never can an authority admit that the intellectually courageous, i.e. those who dare to defy his authority, may be the most valuable type. Of course, the authorities will always remain convinced of their ability to detect initiative. But what they mean by this is only a quick grasp of their intentions, and they will remain for ever incapable of seeing the difference."

Karl R. Popper,
The Open Society and Its Enemies, Volume 1: The Spell of Plato

Contents

Acknowledgments

I would like to dedicate this Doctoral dissertation to all of my family. Their continuous support, counselling and encouragement was the only beacon in the darkness, in critical moments.

I would like to acknowledge Gian Franco Cerofolini which involved me in this project and which unfortunately passed away before the conclusion of the present work.

I would like also to acknowledge Oreste Nicrosini and Guido Montagna for their scientific support, assistance and encouragement, in the final stage of this work, Enrico Prati for useful discussion for the technological aspect, Marco Farina for his contribute to the implementation of the Shrödinger Simulator, and "Fondazione Cariplo" (DOMOS Project) for financial support.

Finally, I would like to thank my girlfriend; I could not have completed this effort without her assistance and tolerance.

Abstract

The present work is divided in two part. The first is dedicated to the investigation of the gas-metal interactions, an interesting area in the basic surface science but also in applied one, since it could provide a more efficient way to design corrosion-resistant structural metals.

In particular, we concentrate our attention on the study H_2S on Fe surface. Experimental studies, of adsorption of H_2S on Fe, and first-principle calculations were carried out for these systems, clarifying some important questions, such as adsorption geometry and dissociation pathways for H_2S, on the above close-packed metal surfaces.

However, real samples will also include a number of defects, in particular step edges where bonding of adsorbates is usually stronger than at facets. It is therefore interesting to investigate adsorption of H_2S on a stepped Fe surface, a task which has not been considered yet to the best of our knowledge.

In the present work we study the H_2S interaction with Fe(310) surfaces by DFT calculations in order to understand the role of step defects in the adsorption properties. We recall that the (310) surface is relatively stable, and its surface energy predicted to be even smaller than that of Fe(110). We do not only obtain the binding sites and adsorption energies of H_2S and its components, but we also relate bonding to the detailed features of the local

density of states (LDOS).

The second part of the present thesis is devoted to the dynamics of scattering. Scattering underlies various physical processes in different field of physics, mainly in solid state, as for example in thermoelectricity, about the filtering of hot electrons by defects, or adsorption and desorption by a surface, or in charge injection and field emission trough interface, usually associated with tunneling mechanisms. The recent developments of nanotechnology and the advent of modern high-speed high-density MOS devices, have revived the technological and theoretical interest of the scientific community on the scattering problem and in particular on quantun tunneling mechanism usually associated. Ultrascaled nanometric CMOS compatible single electron transistors (SETs) and single atom trasistors has lead the emergence of density of states graining and fluctuations in the contacts which may determine discretization of energy levels, charge localization at intradopant length scale and selection rules on quantum states in tunnelling. Consequently, the understanding of dependence of charge dynamics, across a barrier, from the initial position constitutes a relevant aspect in such systems.

In this work we study the scattering process in the non stationary framework using Gaussian wave packet (GWP) to describe the particle wave function of the system so as to consider the dependence of scattering dynamics from the initial conditions. Through a numerical solution of the Schrödinger equation we analyse the evolution of the system calculating the transmission of the scattering GWP as a function of the initial $\sigma_x(0)$ and $x(0)$, and comparing simulated data with theoretical results.

By our analysis a new important issue emerges: the time spent by the particle to reach its asymptotic probability to be observed beyond the barrier (that we call *formation time*), strongly depends on initial conditions, and

in particular on x_0. Finally, to analytically express such a dependence, we propose a semi-classical approximated model in which t_f is described as the time spent by a finite support (accounting for the 0.99 of the probability) of the incident wave packet to cross the barrier, namely the time required to locate, in coordinate space, the greatest amount of the GWP's probability distribution beyond the barrier interface.

The text of this dissertation includes the following previously published material:

- Carone Fabiani F., Cerofolini G.F., Narducci D.,*Dynamics of wave packets generated at a finite distance from a scattering step*, Universal Journal of Physics and Application, Vol.**2**, No.3, 193-199 (2014)

- Carone Fabiani F., Fratesi G., Brivio G.P., *Adsorption of H_2S, HS, S, and H on a stepped Fe(310) surface*, European Physics Journal B, Vol.**78**, 455–460 (2010)

Part

Hydrogen Sulfide H_2S on a stepped Fe(310)

Introduction

The investigation of the gas-metal interactions is an interesting area both in the basic and applied fields of surface science. In particular it could provide a more efficient way to design corrosion-resistant structural metals.

One of the most notorious and aggressive gases is hydrogen sulphide (H_2S), a molecule which is relevant for different reasons. First H_2S is considered as a model molecular system to study the corrosion phenomenon due to sulfur compounds. Owing to the weakness of H-S bond, the barriers for H_2S dissociation, in particular, on transition metals, are usually small [19, 5], leading to fast sulfur deposition on the surface and subsequent sulphide formation. It is well known that adsorbed sulfur acts as poison, for example reducing H_2 dissociation on metals [51], and is also a severe hindrance to hydrogen desorption on transition metals [27]. Also H_2S, a common impurity in fossil derived fuels, has highly poisonous effects on metal based catalysts used in many reactions in petrochemical industry deactivating their catalyzing power. Finally we recall that, once H_2S deposits its hydrogen atoms on the solid, those atoms can also embrittle metals such Ni and Fe [45, 48, 7].

Experimentally, different studies of adsorption of H_2S on close-packed and corresponding open surfaces of transition and noble metals (for example: Co, Cu, Ni, Ir, Pd, Pt, Au, Ag) were performed [53, 32, 9, 29, 46, 22]. They

pointed out the easy dissociation of H_2S on most of these surfaces at low temperatures. In particular, experimental results of adsorption of H_2S on Fe, in a wide range of temperatures, clearly show the absence of molecular free H_2S and HS molecules because of subsequent sulphide formation on the metal surface (see the formation of FeS [37]) at room temperature and below down to about 100 K.

First-principle calculations were also carried out for these systems, clarifying some important questions, such as adsorption geometry and dissociation pathways for H_2S, on the above close-packed metal surfaces [2]. In that work a weakly H_2S molecular adsorption is found, preferentially in the top site with the H_2S molecular plane parallel to the surface. The authors also concluded that a stronger binding occurs on transition metal surfaces than on noble metal ones, following a more facile decomposition of H_2S. In the case of Fe(100), density functional theory (DFT) calculations were performed for characterizing H_2S and HS adsorption [24, 25] and dehydrogenation barriers. Weak adsorption of H_2S at the bridge site with perpendicular orientation to the surface was found. Further calculations reported about the same results for H_2S adsorption on Fe(110) and even lower activation energies for the molecule decomposition [26].

Such (100) and (110) surfaces are among the most stable iron ones [49, 6]. However, real samples will also include a number of defects, in particular step edges where bonding of adsorbates is usually stronger than at facets [44, 31]. It is therefore interesting to investigate adsorption of H_2S on a stepped Fe surface, a task which has not been considered yet to the best of our knowledge.

In the present work we study the H_2S interaction with Fe(310) surfaces by DFT calculations in order to understand the role of step defects in the

adsorption properties. We recall that the (310) surface can be viewed as a stepped (100) one with facets exposing two Fe atoms in between the adjacent steps. It is relatively stable, its surface energy predicted to be even smaller than that of Fe(110) [49]. We do not only obtain the binding sites and adsorption energies of H_2S and its components, but we also relate bonding to the detailed features of the local density of states (LDOS) [18, 8].

In chapter 2 we present the theoretical background for our analysis with particular focus on Density Functional theory (DFT). In chater 3 we describe the computational method used in this study. In particular, in section 3.2, after presenting our results for adsorption on Fe(100) which will serve as reference, we show bonding energies, geometries and the LDOS's for adsorption of H_2S and HS on Fe(310), providing also the same analysis for H and S adatoms following the dissociation of the previous species. The last section is devoted to the conclusions.

- Chapter 1 -

Density Functional Theory

This chapter is devoted to a brief overview of first-principles techniques, in solid state physics, used in our analysis. The first part of this chapter we describe the theoretic approach to the many-body problem in solid state physics (the Born-Oppenheimer approximation) used to study the properties of materials at the atomic scale. Then we present the fundamentals of Density Functional Theory (DFT) and the practical numerical implementation used in the present study: pseudopotentials, k-point sampling, supercell.

§ 1.1 Many-body problem

The starting point to study of the physics of a time-independent quantum system of interacting particles is the application of the following Schrödinger equation:

$$H\Psi = E\Psi \tag{1.1}$$

where H is the Hamiltonian of the system, Ψ is the wave function describing all the particles of the system and E is the corresponding energy. In solid state physics, systems are described in terms of interacting electrons and nuclei with the following Hamiltonian:

$$H(\mathbf{R},\mathbf{r})\Psi = T_{\mathrm{N}}(\mathbf{R}) + T_{\mathrm{e}}(\mathbf{r}) + V_{NN}(\mathbf{R}) + V_{ee}(\mathbf{R}) + V_{\mathrm{eN}}(\mathbf{R},\mathbf{r}) \tag{1.2}$$

where $\mathbf{R} \equiv \mathbf{R}_I$ labels the set of all the nuclear coordinates $\mathbf{R}_I$ and $r \equiv \mathbf{r}_i$ labels the set of all the electronic coordinates $\mathbf{r}_i$. T_{N} and T_{e} are respectively the kinetic energy operator of nuclei and electrons, V_{NN}, V_{ee}, V_{eN} are the Coulomb electrostatic potential energy operators between respectively nuclei, electrons, and electrons and nuclei:

$$T_{\mathrm{N}} = -\frac{\hbar^2}{2}\sum_I \frac{1}{M_I}\frac{\partial^2}{\partial \mathbf{R}_I^2} \tag{1.3}$$

$$T_{\mathrm{e}} = -\frac{\hbar^2}{2m}\sum_I \frac{\partial^2}{\partial \mathbf{r}_i^2} \tag{1.4}$$

$$V_{NN} = \frac{e^2}{2}\sum_{I\neq J}\frac{Z_I Z_J}{||\mathbf{R}_I - \mathbf{R}_J||} \tag{1.5}$$

$$V_{ee} = \frac{e^2}{2}\sum_{i\neq j}\frac{1}{||\mathbf{r}_i - \mathbf{r}_j||} \tag{1.6}$$

$$V_{eN} = -e^2\sum_{i\neq I}\frac{Z_I}{||\mathbf{r}_i - \mathbf{R}_J||} \tag{1.7}$$

where Z_I is the charge of ion I with mass M_I, m is the mass of the electron and e its elementary charge. The widely used approximation to deal with (1.2) is the Born-Oppenheimer approximation [4] which enables to decouple the nuclear degrees of freedom from the electronics ones. In such an approximation, the large nuclei masses can be considered as stationary compared to the electric charges such that the kinetic energy (1.3) of the nuclei is treated as a perturbation on the electronic Hamiltonian H_{e}:

$$H_{\mathrm{e}}(\mathbf{R},\mathbf{r})\Psi = T_{\mathrm{e}}(\mathbf{r}) + V_{\mathrm{NN}}(\mathbf{R}) + V_{\mathrm{ee}}(\mathbf{R}) + V_{\mathrm{eN}}(\mathbf{R},\mathbf{r}). \tag{1.8}$$

where the set of atomic positions $\mathbf{R}$ can be treated as fixed parameters in H_{e}. In this context, the potential energy V_{eN}, due to the interaction of the nuclei on the electrons, can be seen as the energy of the electrons in the fixed external potential of the nuclei. Once the potential V_{ee}, V_{eN} and V_{NN} are computed, the quantum description of a solid is obtained through the Schrödinger equation and its solution $\Psi(\mathbf{r})$ as a many-body electronic wave function. Hence, the electronic wave function, electronic density and the eigenstates of any operator can be calculated at different nuclear positions. Moreover, the ionic geometry of the system can be obtained by computing the forces (Hellmann-Feynman theorem [11]) and stresses (generalized Virial theorem [38]). However, the many-body wave function remain a complicated quantity depending on $3N$ spatial variables and $3N$ spin variables. The huge number of variables, increasing with N, severely limits the sizes of a system when it is treated with wave function based methods, so, for practical calculation, it is necessary to adopt a different paradigm as proposed by Density Functional Theory.

§ 1.2 Density Functional Theory

Due to their high computational efficiency and accuracy, DFT methods have become the most widely used ab-initio methods in solid state physics to describe the interacting systems of molecules, crystals and surfaces, also providing a simple method for describing the effects of exchange and correlation in an electron gas. In contrast with wave function based methods, the central quantity in DFT approach is the electronic charge density distribution $\rho(\mathbf{r})$. Moreover, with respect to both the approximated Thomas-Fermi and Hartree-Fock-Slater methods, DFT has the advantage to be in principle ex-

act for the ground state. In their pioneering works, Hoemberg and Kohn [20] showed that the minimum of the total energy as a functional of $\rho(\mathbf{r})$ is the ground state energy of the system, and that the minimum value of $\rho(\mathbf{r})$ is the exact single-particle ground-state density. After that, Kohn and Sham showed that a many-electron problem can be replaced by a fictitious non interacting particles problem solvable by an equivalent set of self-consistent one-electron equations, in which the ground state properties of the system are functionals of the ground state electron density [30]. The equations derived by the Hoenberg-Kohn-Sham approach are time-independent Schrödinger-like equations in which the electron-electron interaction potential is split for convenience into two parts: the Hartree potential, and an exchange-correlation potential, whose form is, in general, unknown. The advantage of using the electron density over the wave function is reducing dimensionality. In fact, the density is always 3 dimensional whatever is the number of electrons contained in the system enabling DFT to deal with a much larger systems than others methods. In the next sections, we will give a basic introduction to DFT(see [30, 55, 12, 28] and textbooks [39, 10] for further reading)

§ 1.3 The Hohenberg-Kohn theorems

Herein we provide the proofs of the main results due to the work of Hohenberg and Kohn that can be summarized as follows: (i) there is a one to one mapping between external potential and electron density; (ii) the ground state density exists can be found trough a variational principle. Reducing our attention on a non-degenerate systems, we suppose to deal with an electronic system interacting trough an external potential $v(\mathbf{r})$. We assume that we

know the electron density of this system which determines $v(\mathbf{r})$ and thus all its properties. Suppose another external potential $v'(\mathbf{r})$ exists which differs from $v(\mathbf{r})$ but with the same electron density ($\rho\mathbf{r}$) for the ground state. So we will have two different Hamiltonians $\hat{H}$ and $\hat{H}'$ whose ground state electron density is the same but the normalized wave function Φ and Φ' would be different. How we will see this leads to a contradiction. In fact we can write:

$$\begin{aligned} E_0 < \langle|\Phi'|\hat{H}|\Phi'\rangle &= \langle|\Phi'|\hat{H}'|\Phi'\rangle + \langle|\Phi'|\hat{H} - \hat{H}'|\Phi'\rangle \\ &= E'_0 + \int \rho(\mathbf{r})[v(\mathbf{r}) - v'(\mathbf{r})]\mathrm{d}\mathbf{r} \end{aligned} \tag{1.9}$$

where E and E' are the ground-state energies for $\hat{H}$ and $\hat{H}'$, respectively. Similarly we can get

$$\begin{aligned} E'_0 < \langle|\Phi|\hat{H}|\Phi\rangle &= \langle|\Phi'|\hat{H}'|\Phi'\rangle + \langle|\Phi'|\hat{H}' - \hat{H}|\Phi'\rangle \\ &= E_0 - \int \rho(\mathbf{r})[v(\mathbf{r}) - v'(\mathbf{r})]\mathrm{d}\mathbf{r} \end{aligned} \tag{1.10}$$

Adding (1.9) and (1.10), we will obtain the following false relation:

$$E_0 + E'_0 < E'_0 + E_0. \tag{1.11}$$

Hence it is impossible to have two different external potentials with the same $\rho(\mathbf{r})$. Thus $\rho(\mathbf{r})$ uniquely determines $v(\mathbf{r})$ and all ground state properties.

The second Hohenberg-Kohn theorem demonstrates that the ground state energy can be obtained variationally, where the exact ground state density is the density that minimize the total energy. It means:

$$E_0[\rho] \leq E[\rho] \tag{1.12}$$

First, rewriting the energy E as a function of the electron density only,

we have: $\rho(\mathbf{r})$:

$$E[\rho] = T[\rho] + T_{\text{ne}}[\rho] + V_{\text{ee}}[\rho] \tag{1.13}$$

$$= \int \rho(\mathbf{r})v(\mathbf{r}) + F_{\text{HK}}[\rho] \tag{1.14}$$

where

$$F_{\text{HK}}[\rho] = T[\rho] + V_{\text{ee}}[\rho] \tag{1.15}$$

Note that $F_{\text{HK}}[\rho]$ is function only on ρ and independent by any external potential $v(\mathbf{r})$. Thus $F_{\text{HK}}[\rho]$ is a universal functional of ρ Assuming the first theorem, the ρ uniquely defines the external potential $v(\mathbf{r})$, hence, for any other wave function Φ' and its electron density ρ', we have:

$$\langle|\Phi'|\hat{H}|\Phi'\rangle = \int \rho'(\mathbf{r})v(\mathbf{r}) + F_{\text{HK}}[\rho] \equiv E[\rho'] \geq E[\rho] \tag{1.16}$$

So the energy will reach the minimum only when the electron density is the ground-state electron density, which proofs the thesis.

§ 1.4 The Kohn-Sham Equations

Although the Hohenberg-Kohn theorem provided the connection between the ground state density and the total energy of the system the problem on how to obtain the density $\rho(\mathbf{r})$, or the functional $F_{\text{HK}}[\rho(\mathbf{r})]$, remained an unsolved problem. Later, Kohn and Sham [30] resolved the problem by introducing the one electron orbitals and approximating the kinetic energy of the system by the kinetic energy of non-interacting electrons. In such a way they got the following equation which represents the central equation in Kohn-Sham DFT:

$$\left(-\frac{1}{2}\nabla^2 + v(\mathbf{r}) + \int \frac{\rho(\mathbf{r})}{|\mathbf{r}-\mathbf{r}'|}\mathrm{d}\mathbf{r} + v_{\text{xc}}(\mathbf{r})\right)\phi_i = \epsilon\phi_i \tag{1.17}$$

where, on the left hand side, the kinetic energy of the non-interacting reference system, the external potential, the Hartree potential, and the exchange-correlation potential, respectively appears.

If we set:

$$v_{\text{eff}}(\mathbf{r}) = \int \frac{\rho(\mathbf{r}')}{|\mathbf{r} - \mathbf{r}'|} \mathrm{d}\mathbf{r}' + v_{\text{xc}}(\mathbf{r}) \tag{1.18}$$

we obtain a more compact form of (1.17),

$$\left(-\frac{1}{2}\nabla^2 + v_{\text{eff}} \right) \phi_i = \epsilon \phi_i \tag{1.19}$$

As we can see, (1.19) is the one-electron Schrödinger-like equation. Here, ϕ are the Kohn-Sham orbitals, ϵ is its energy and the electron density is:

$$\rho(\mathbf{r}) = \sum_i |\phi_i|^2 \tag{1.20}$$

and the exchange-correlation potential is expressed by:

$$v_{\text{xc}} = \frac{\delta E_{\text{xc}}[\rho]}{\delta \rho(\mathbf{r})} \tag{1.21}$$

where $E_{\text{xc}}[\rho]$ is the exchange-correlation functional which is not known and in which it is discharged all the lack of information of the original system.

Equations (1.19), (1.20), and (1.21) compose the Kohn-Sham equations. Note that the v_{eff} depends only on $\rho(\mathbf{r})$ through (1.18). The Kohn-Sham equations represent a mapping of the interacting many-electron system onto a system of non interacting electrons moving in an effective potential due to all the other electrons. They must be solved self-consistently. The general procedure to solve the Kohn-Sham problem is described as follows: an initial trial electron density is settled to construct the v_{eff} from (1.18). As a result the Kohn-Sham orbitals are obtained. Based on these orbitals, a new density is obtained from (1.20) and the process repeated until convergence is

achieved. Finally, the total energy will be calculated by final electron density through the following:

$$E = \sum_{i}^{N} \epsilon_i - \frac{1}{2} \int \int \frac{\rho(\mathbf{r})\rho(\mathbf{r}')}{|\mathbf{r} - \mathbf{r}'|} \mathrm{d}\mathbf{r}\mathrm{d}\mathbf{r}' + E_{\mathrm{xc}}[\rho] - \int v_{\mathrm{xc}}(\mathbf{r})\rho(\mathbf{r})\mathrm{d}\mathbf{r}. \tag{1.22}$$

In principle, once each term in the Kohn-Sham energy functional was known, the exact ground state density and total energy are obtained. Unfortunately, the exchange-correlation E_{xc} functional is not exactly accessible and it is necessary to approximate it to deal with the Kohn-Sham equations. E_{xc} includes the non-classical aspects of the electron-electron interaction along with the component of the kinetic energy of the real system different from the fictitious non-interacting system. Different approximations for E_{xc} have been used, with varying levels of complexity [43].

§ 1.5 Generalised Gradient Approximation (GGA)

As we can see from (1.21), the exchange-correlation potential v_{xc} is a functional derivative of the exchange correlation energy with respect to the local density. For a homogeneous electron gas, this will only depend on the value of the electron density, while for a non homogeneous system, the value of v_{xc} at the point $\mathbf{r}$ depends also on its variation close to $\mathbf{r}$.

So, the exchange-correlation potential v_{xc} can be expanded in terms of the gradients of the density:

$$v_{\mathrm{xc}}[\rho(\mathbf{r})] = \mathbf{v}_{\mathrm{xc}}[\rho(\mathbf{r}), \nabla\rho(\mathbf{r}), \nabla(\nabla\rho(\mathbf{r})), ...] \tag{1.23}$$

As the exact form of the energy functional is unknown, different approximations for v_{xc} can be deduced considering increasing order of the gradient

of the density into the definition. Following Perdew-Schmidt "Jacob's ladder" [43], it is possible to classify the the exchange-correlation functional as follows:

- LDAs (first rung), which depends only on the local density,
- GGAs (second rung) in which the dependence on the gradients of the density is added,
- MGGAs (third rung), including Laplacian of the density and/or the (local) Kohn-Sham orbital kinetic energy density,
- Hybrid functionals (fourth rung), in which the exact exchange is added to the MGGAs functionals
- the fully non-local functionals (fifth rung), which make use the unoccupied kohn-Sham orbitals also.

In te present thesis we take into account GGAs functionals, which takes into account the density $\rho(\mathbf{r})$ and the its gradient:

$$E_{\mathrm{xc}}^{\mathrm{GGA}}[\rho(\mathbf{r})] = \int \rho(\mathbf{r})\epsilon_{\mathrm{xc}}^{\mathrm{GGA}}\rho(\mathbf{r})\nabla\rho(\mathbf{r})\mathrm{d}\mathbf{r} \tag{1.24}$$

So called semi-local GGAs functionals are more suitable approximations than the LDAs functionals for the study of many properties, for example geometries and ground state energies of molecules, while they are not necessarily better than LDA with relation to the properties of metals and their surfaces. The most widely used GGAs in surface physics are the PW91 [41] and PBE [40] family of functionals. Others popular funtcionals as PBE, revPBE [54], RPBE [17], PBE-WC [52], and PBEsol [42] belong to this family. RPBE is the most popular of them, although PBE-WC and PBEsol, seem to be promising methods for the simulation of solids and their surfaces. Finally,

the AM05 functional [3], designed to include surface effects has been shown to offer a much improved performance for lattice constant and bulk modulus than PBE [35].

§ 1.6 Plane-Wave Basis Sets

In practical DFT calculations of solids or condensed matter, one must adopt a basis set of wave functions and plane-wave basis set is a very widely used choice. We will now briefly discuss plane-waves and then the pseudopotential methods usually adopted jointly with plane-waves for treating the strong interactions between core electron and nuclei.

Crystal is a periodically arranged structure of atoms, whose electrons lie in a periodic external potential $U(\mathbf{r})$ with the same periodicity as the underlying Bravais lattice $\mathbf{R}$, it means:

$$U(\mathbf{r}+\mathbf{R}) = U(\mathbf{r}) \tag{1.25}$$

For an infinite solid with the Born-Von Karman periodic boundary conditions, Bloch's theorem [4] asserts that, the eigenstates ϕ of the one electron Hamiltonian with potential $U(\mathbf{r})$ can be written as

$$\phi_{nk}(\mathbf{r}) = \exp(i\mathbf{k}\cdot\mathbf{r})u_{nk}(\mathbf{r}) \tag{1.26}$$

where u_{nk} have the same periodicity as the potential ($U(\mathbf{r})$). Furthermore, u_{nk} can be expanded as,

$$u_{ik} = \frac{1}{\Omega_{\text{cell}}}\sum_m c_{i,m}\exp(iG_m\cdot\mathbf{r}) \tag{1.27}$$

where G is the reciprocal lattice vector and $\Omega = N_{\text{cell}}\Omega_{\text{cell}}$, with Ω as the whole volume.

By inserting (1.27) in (1.26), the eigenfunctions can be written as

$$\phi_i(\mathbf{r} = \sum_q c_{i,q} \frac{1}{\sqrt{\Omega}} \exp(i\mathbf{q} \cdot \mathbf{r}) \tag{1.28}$$

Here $c_{i,q}$ are the expansion coefficients, $\mathbf{q} = \mathbf{k} + G$, and the exponential terms in (1.28) are the basis of the orthonormal plane-waves.

Obviously, this Fourier transform of the Bloch functions involves infinite number of plane waves to exactly describe them, so, in practice, the plane wave expansion is truncated to the plane wave with energy lower than a certain cut-off energy E_{cut} and convergence studies must be performed to choose suitable cut-off, depending on the system and on desired precision.

1.6.1 Brillouin zone grid

Generally, calculations on the reciprocal space involve the knowledge of the Bloch functions over an infinite $\mathbf{k}$ points over the Brillouin zone. So, practically, we need to select a finite number of $\mathbf{k}$ points where the Bloch functions are known. In this thesis we will use the Monkhorst and Pack [36] technique to sample the reciprocal space which allows to define a finite mesh of $\mathbf{k}$ points in each direction, as a good compromise between computational cost and accuracy of the results. This set of $\mathbf{k}$-points depends on the symmetry of the system and must be converged in each case study by increasing its size.

§ 1.7 Pseudopotentials

As we have seen before, to perform numerical calculations we must to truncate the plane wave expansion on the base of some cut-off energy criterion. Unfortunately, two main problems arise: the deeply bound core electrons require a huge amount of basis functions for their correct description [33], and

second the valence electron wave function in the core region suffer of rapid oscillations. So, we run into the problem to have a good description of such electrons by an acceptable computational cost

The pseudopotential approach [14] is devoted just to such a problem and it is based on the two following approximations. The first consists in considering the electronic properties of the molecules and solids mainly due by the valence electrons while the core electrons can be considered as frozen. On the other hand, it is expected that the core electrons that do not directly involved to the chemical bonding are only slightly affected by modifications of the atomic environment.

The second approximations is to replace a smooth version of the nucleus potential (the so called "pseudo-potential"), as the central region of the valence electronic wave functions is weakly involved in the chemical properties of the atoms. The atomic potential, screened by the core electrons, is replaced by a pseudo potential such that the analytical form of the valence wave functions don't change beyond a given cut-off radius and are replaced by smoothly varying function in the core region. The above approximations allow to reduce the number of electrons, and the respective plane waves, involved in the Kohn-Sham equations and hence the computational cost. Among many types of pseudopotential developed for DFT calculations in the last year [50] we adopted the pseudopotential implemented in QUANTUM ESPRESSO code used for our calculations.

- Chapter 2 -

Adsorption of molecules on Metal Surfaces

Adsorption mechanism and surface reactions are the main aims of surface science. In particular the nature and the energetics of adsorption , the geometries and the bond lengths of the adsorbate represent the core of the surface and interface analysis. DFT is one of the most powerful tool for analysing surface geometries, to calculate adsorption energies, as well electronic and atomic structures. DFT calculations describe the geometry and energy differences of chemically similar bound adsorbates with a very good accuracy, but it is less precise to predict absolute energy.

§ 2.1 Adsorption process

When atoms or molecules in the gas phase (called the adsorbates) and a solid or liquid surface (called the substrate) brought together, they start to interact. Adsorption is the process which describes the binding of an adsorbate on a substrate. The inverse process of removing the adsorbate from the surface is called desorption. It is possible to distinguish the adsorption phe-

nomenon in two classes [47]: physisorption and chemisorption. Physisorption refers to the adsorption in which a weak intermolecular bonding as Van der Waals between adsorbate and substrate are involved and which is related to adsorption energies typically less than 0.3 eV per particle. Due to this weak interaction, a small perturbation electronic structure of the adsorbate is expected. Chemisorption refers to those processes where the adsorption energy is larger, characterized by a chemical bond (covalent bond) between the adsorbate and the surface. In this case the electronic structure of adsorbate is significantly modified.

The nature of the adsorbate-surface bond varies significantly with the substrate. Besides being a reservoir of ions a surface has the effect to stabilize intermediates and hence to catalyze reactions and also to allow defect grow.

On metals, the largest contribution to bonding comes from an interaction with the conduction band [21], which shares electrons with the adsorbate, modifying the electron density of the neighbourhood of the adsorbate [34].

The adsorbate wave functions are hybridized and the interaction with s-band states of the substrate causes a broadening of the adsorbate levels. The broadening and shifting to the substrate Fermi level of electronic levels of an adatom close to the surface, is due to the spill out of the substrate s-electrons mostly into the vacuum [47]. Broadening implies a coupling of the electrons of the adatom, which are localized, to the substrate, leading to a delocalization. The more localized d-states also interact with the atomic levels. In this case the narrow d-band interacting with the atomic levels mix and split into bonding and antibonding states. The bonding state, with a lower energy, is due to those states which have an increased electron density between the adsorbate and the substrate, while the higher energy antibonding state, which is due to those states with a node between the adsorbate and

the substrate. Moreover, due to the hybridization with the adsorbate, the electron density inside the d-band decreases and move to higher and lower energy band, and the resulting adsorbate-surface DOS, shows peaks close to the lower and upper edge of the d-band. The bonding is strongest when bonding states are occupied and antibonding states remain empty.

Based on the assumption that trends in the chemisorption energy of the adsorbate-surface strictly depends by the interaction of adsorbate orbitals with surface sp- and d-bands, a simplified theory of adsorbate bonding on transition metal surfaces has been proposed by Hammer and Norskov [18, 15, 16]. In particular the change in the energy due to the hybridization of the adsorbate orbital with the d-bands of metals is equal to the corresponding changes in chemisorption energy. Their in-depth analysis of the adsorbate-induced change in the density of states shows two basic features: (i)the coupling to the d-states can be reduced to a two level problem (bonding and anti-bonding states), and (ii) the basic feature to characterize d-bands is the their band center. The general trends for the transition metals are that: going to the left in the Periodic Table, the bonds become stronger as the d-band is emptying, and they become weaker going down the Periodic Table. Some important correlation for the adsorption of isolated atoms on metallic surfaces is that stronger bonding, go together with shorter bondlengths. For sites with lower coordination than hollow adsorption site, the strength per bond will typically increase, because the same number of adsorbate electrons have to be distributed over fewer bonds, resulting to a decrease of the bond length on top and bridge sites. This correlation between local coordination and bond strength, and the correlation between bond strength and bond length is well known.

§ 2.2 Potential Energy Surfaces, Adsorption Energy

The total energy $E_{total}(V, N_A^{\text{nuc}}, N_B^{\text{nuc}}, ..., \mathbf{R}_I)$ of an atomic arrangement in the Born-Oppenheimer approximation can be described as an hypersurface, in the atomic coordinates space, called PES [47]. Once its expression is obtained, for example by a DFT calculation its global minimum represent the most stable configuration of the system.

The adsorption energy per atom is the difference of the total energy of the adsorbate system and the total energy of the clean substrate, as follows:

$$E_{\text{ads}} = -(E_{\text{total}} - E_{\text{clean/surface}} - NE_{\text{adatom}})/N \tag{2.1}$$

where E_{total} is the total energy per adatom, $E_{\text{cleansurface}}$ is the total energy of the clean substrate, and NE_{adatom} is the total energy of N free adsorbates involved in the adsorption process.

§ 2.3 Surface models

2.3.1 Structure and modelling of clean surfaces

Surfaces are generated cleaving a bulk crystal. In such a way atoms at the surface modify decreasing their coordination degree with respect to those in the bulk. This cause a relaxation and eventually the reconstruction of the atoms at the surface with a change of the surface geometry and a new equilibrium atomic positions is reached. Considering an ideal cubic crystals, is possible to distinguish two classes of surfaces: flat surfaces with low Miller

index ((100), (111) and (110) surfaces), and stepped surfaces with higher Miller index.

However, although an ideal flat surface can be consider a good model providing relevant informations about real samples, such systems also include a number of defects, such as kinks, vacancies or steps, which could drastically modify the properties of the substrate with respect to an ideal one.

To better understand the adsorption of H_2S on a real Fe surface in this thesis we will concentrate our attention on stepped surfaces. Steps can be suitably implemented using vicinal surfaces, which exhibit a regular array of steps. Vicinal surfaces (or stepped surfaces or high-Miller-index surfaces)can be created by cleaving a crystal at a small angle away from a low-Miller-index plane. Vicinal surfaces exhibit atomic terraces with a low-index orientation, and these terraces are separated by atomic steps.

In the present work we use an Fe(310) surface, which exhibit different sites with a similar symmetry but involving different kinds of Fe atoms.

2.3.2 Supercell approach

Supercell model is one of the most widely adopted approach for surface simulations especially for metal surfaces with de-localized valence wavefunctions.

Supercell approach implies the use of slabs and vacua. The slab in the supercell is infinite and periodic in the directions parallel to the surface, but finite in the direction perpendicular to the surface to assure the correct dispersion of the band formation. Constructing supercell model one must pay attention to the following criteria: the thickness of the slab must be sufficient to avoid interaction between the two surfaces of the slab and the vacuum thickness must be large enough to avoid mutual interactions between surfaces of consecutive slabs. This procedure also guarantees that the middle

Figure 2.1: *Slab structure*

layers of the slab show bulk-like properties. In our study we just use a slab vicinal surface model in the supercell approach to investigate the properties of vicinal surfaces.

We choose a reasonable surface unit cell size, constructing the slab from the corresponding high Miller-index plane layer by layer, paying a particular attention on proper k-point sampling. Such a setup allows the investigation of long-range step-step interactions.

- Chapter 3 -

Adsorbtion of H_2S, HS, S, and H on a stepped Fe(310)

This chapter contains setting, procedures and results of the first-principle calculations performed to simulate the adsorbtion of the hydrogen sulfide molecule on a stepped Fe(310) surface, and all the species composing H_2S: HS, S, and H. We will provide energy and geometry of all such the species with particular attention on the most stable configurations

§ 3.1 Simulation setting

We perform first-principle calculations based on spin-polarized DFT [20, 30]. To solve the Kohn-Sham equations, with periodic boundary conditions and a plane-waves basis set, we use the Quantum Espresso (Q.E.) integrated suite of codes [13]. We use the generalized gradient approximation(GGA) of PBE to treat the electron exchange and correlation[40], using pseudopotentials available in the Q.E. website. The Kohn-Sham one electron valence eigenstates were expanded in terms of plane-wave basis sets with a cut-off energy

of 220 Ry. We use the first order Marzari-Vanderbilt method for the Fermi surface smearing with a width of 0.02 Ry and the Monkorst-Pack scheme for k-point sampling of the Brillouin zone, with a converged k-mesh of 8×8×8 for bcc Fe. First we determine the equilibrium lattice constant a_0 for the ferromagnetic bcc Fe. The resulting value for a_0 is 2.84 Å in good agreement with the experimental one equal to 2.86 Å [1]. To calculate the electronic structure of the isolated species H_2S, HS, S, and H we set the molecules and the atoms in a 11.36 Å periodic cubic box.

Following a convergence study of the total energy, we chose a 5-layer slab to model the Fe(100) surface and a 8-layer slab for Fe(310), in order to consider a thickness for the latter as close as possible to the that of the Fe(100) slab. In the case of Fe(100) the top two layers of the substrate were allowed to relax together with the adsorbate layer deposited on that side of the slab. The bottom three layers were kept fixed in their bulk positions to represent the semi-infinite crystal. In the case of Fe(310), the top three layers of the substrate were allowed to relax and the bottom five ones were kept fixed in the bulk positions. A (2×2) surface unit cell at 0.25 monolayers (ML) coverage was adopted for studying adsorption on Fe(100). A coverage as close as possible to that value was considered for Fe(310), namely 0.30 ML in a (2×1) surface unit cell. We use a 4×4 k-mesh for both Fe(100) and Fe(310) surfaces, which determines the adsorption energy of H_2S within $5 \cdot 10^{-6}$ Ry.

The adsorption energy of each species was obtained by the equation:

$$E_{\text{ads}} = E_{\text{sys}} - E_{\text{slab}} - E_{\text{mol}}, \tag{3.1}$$

where E_{sys}, E_{slab}, and E_{mol} are the total energy of the whole system (adsorbates and slab), of the Fe slab, and of the isolated molecule or atom, respectively. Following common practice, we take half the calculated energy

for an H_2 molecule as value of E_{mol} for H species.

§ 3.2 Results and discussion

In this section we report all our results and analysis relative to the adsorption of all the species possibly involved in the interaction of H_2S and both the Fe(100) and Fe(310) substrate, eventually analysing and also comparing their the Local Density of States (LDOS). Remind that LDOS is a key quantity to analyse the electronic structure and system properties, such as the valence band, conduction band, Fermi energy, bonding region, etc. It is the number of electronic states within energy between E and $E + dE$, defined as:

$$n(r, \epsilon) = \sum_i |\psi_i(r)|^2 \delta(\epsilon - \epsilon_i) \tag{3.2}$$

where $\psi_i(\mathbf{r})$ is the single-particle Kohn-Sham eigenfunction, and ϵ_i the corresponding eigenvalue.

Before studying the adsorption features of each species, we must distinguish different high-symmetry sites on the two surfaces. In the case of Fe(100) (see Figure 3.1(a)), there are bridge (b), hollow (h) and top (t) sites. On the Fe(310) surface (see Figure fig:1(b)), we can distinguish different sites having the same similar symmetry but involving different kinds of Fe atoms. Indeed, top-layer Fe atoms at the step edge have 4 nearest neighbours (NN) as in the (100) surface, while those at the second layer (at the bottom of the step) have 6 NN. Hence we have a four-fold hollow site ($4h$) on the (100) facets and two kinds of three-fold hollow site at the surface step. The first one, which we denote by ($3h_1$), involves two Fe atoms at the step edge and one at the bottom of the step. Conversely, the second one, labelled by ($3h_2$), involves one Fe atom at the step edge and two ones at the bottom. Finally

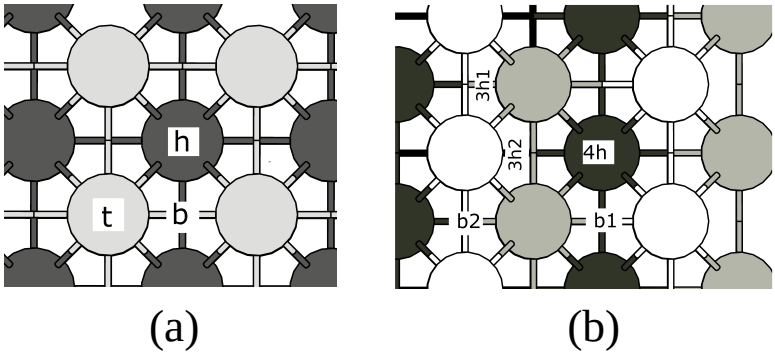

Figure 3.1: *Ball-stick view of Fe(100) (panel (a)) and Fe(310) (panel (b)) with labelled high-symmetry sites. Brighter circles denote higher Fe atoms.*

two different kinds of bridge sites are present, on the terraces and on the step edges, denoted by (b_1) and (b_2), respectively.

The LDOS of the outermost Fe atoms is plotted in Fig. 3.2 where panel (a) shows the LDOS for the first layer of Fe(100), panel (b) the one of the Fe atoms at the top of the step edge of Fe(310), and panel (c) the one of the Fe atoms at the bottom of the step. We find that the band edges are very similar and that from the bottom to the Fermi level they integrate to about the same value (7.80 and 7.82 e^- for topmost atoms in Fe(100) and (310), respectively). The following quantitative differences are found and we expect a corresponding effect to binding energies. In fact the weighed centre of the d band at the outermost Fe atom increases from -1.34 eV for Fe(100) to -1.19 eV for Fe(310). We also found that the LDOS at the Fermi level is smaller for the stepped than for the flat surface: 0.82 eV^{-1} and 1.21 eV^{-1}, respectively, though this does not imply a lower reactivity for the latter one[15].

In Tab. 3.1 we present the results of the adsorption energy, bond distances and geometry for all the species considered in the case of Fe(100). As we can see our results are in good agreement with previous theoretical investigations, especially concerning the energies of the most stable adsorption sites, which

differ by 0.05 eV from those of Ref.[25, **?**] at most.

Binding energies and structural details for the various species on Fe(310) are reported in Tab. 3.2 and will be now discussed. In this case, since some adsorption sites relax to the same adsorption coordinates during our structural optimization, such equivalent results are shown only for the adsorbate site closer to the final geometry.

3.2.1 H and S Adsorption on Fe(310)

For H adsorption, the results indicate a larger binding energy (-0.54 eV) and a more stable position in the ($3h_1$) site. All sites, except (b_1), are equally or more stable with respect to the similar ones of the Fe(100) surface, whose binding energy in the most stable site (hollow), is -0.34 eV. The same ($4h$) site is preferred by S (adsorption energy equal to -5.77 eV) on Fe(310)) as on Fe(100), even if the adsorption magnitude is now smaller, since it amounts to -5.97 eV on the flatter surface.

The above results can be understood in a better way by looking at the LDOS of the two species summed on the spin populations. Figure 3.3 shows the LDOS of the whole system (slab plus adatom) projected onto the s state of the H atom on Fe(100) lying in the hollow site (panel (a)), and on Fe(310) in the $3h_2$ hollow site (panel (b)). In both cases, the total ($d + s$) LDOS of the topmost Fe atoms of the clean surfaces (that in panel (a) of Fig. 3.2, shaded area) is reported as reference. We verified that such LDOS does not change substantially in presence of the adsorbate. Following the generalized Grimley-Anderson-Newns theory of chemisorption [8, 18, 15] the interaction of the adatom state with the d states of the metals determines a bonding and an anti-bonding state (the latter usually smeared out in the valence band). The former becomes a resonance owing to the interaction with the s band

Table 3.1: *H_2S, HS, S and H adsorption energy, bond length, and HSFe and HSH angles on Fe(100) calculated in the present work (a), and reported in Ref.[25, 23] (b).*

		bridge(a)	hollow(a)	top(a)
H_2S	E_{ads}[eV]	-0.39	-0.10	-0.29
	$R_{\mathrm{S-H}}$ [Å]	1.357	1.374	1.363
	$\Theta_{\mathrm{HSH}}[deg]$	92.8	92.1	91.6
HS	E_{ads}[eV]	-3.13	-3.35	-2.61
	$R_{\mathrm{S-H}}$ [Å]	1.365	1.393	1.358
	$\Theta_{\mathrm{HS/Fe}}[deg]$	64.7	1.2	71.0
S	E_{ads}[eV]	-4.78	-5.97	-4.00
H	E_{ads}[eV]	-0.28	-0.34	0.26
		bridge(b)	hollow(b)	top(b)
H_2S	E_{ads}[eV]	-0.46	-0.13	-0.33
	$R_{\mathrm{S-H}}$ [Å]	1.373	1.399	1.362
	$\Theta_{\mathrm{HSH}}[deg]$	91.7	86.5	93.6
HS	E_{ads}[eV]	-3.30	-3.56	-2.76
	$R_{\mathrm{S-H}}$ [Å]	1.363	1.393	1.395
	$\Theta_{\mathrm{HS/Fe}}[deg]$	58.9	0.00	80.5
S	E_{ads}[eV]	-4.79	-6.00	-4.06
H	E_{ads}[eV]	-0.32	-0.38	0.23

Table 3.2: *H_2S, HS, S and H adsorption energy, bond length, and angles on Fe(310) calculated in the present work.*

		b_1	b_2	$3h_1$	$3h_2$	$4h$
H_2S	E_{ads}[eV]	-0.24	-0.45	-0.24		
	R_{S-H} [Å]	1.377	1.378	1.381		
	$\Theta_{HSH}[deg]$	92.6	91.9	90.9		
HS	E_{ads}[eV]		-3.29			-3.22
	R_{S-H} [Å]		1.361			1.391
	$\Theta_{HSH}[deg]$		75.8			15.7
S	E_{ads}[eV]	-4.68		-5.38		-5.77
H	E_{ads}[eV]	-0.14		-0.54	-0.33	-0.38

of the metal. Hence both on Fe(100) and on Fe(310) we can observe that the s state of H broadens. We note that, passing from the flat case to the stepped one, the hydrogen LDOS slightly shifts towards higher energies being more hybridized with the Fe valence states, with increased magnitude of the bonding energy of H by 0.20 eV on Fe(310) than on Fe(100). Such an effect can be explained by close examining the equations for the d hybridization in chemisorption in refs.[8, 15, 16], which show that bonding energy increases by increasing the energy difference between the adatom orbital and the weighed average d band energy.

In Fig. 3.4 we plot the total LDOS of the system, projected separately onto the s and p states, of the adsorbed S in the four-fold hollow sites on both Fe(310) and Fe(100) surfaces. Also in this case, we display the projected LDOS onto d and s states of the metal atoms before adsorption. For both surfaces, at the lowest energies we can observe a narrow peak corresponding

to the s state of sulfur atom, which does not hybridize with the Fe states. Then, the adatom p state resonances, closer to the Fermi level, are found. For both s states and p states of sulfur there is an energy shift towards lower values, passing from the (100) surface to the (310) one. Hence the p peaks of sulfur for the flat surface are closer to the Fermi level with to a larger hybridization between adsorbed S and metal states on the (100) surface.

The above consideration about the atomic H and S species can be summarized as follows. There is a common trend for the LDOS of adsorbed species: larger magnitudes of adsorption energy correspond to a shift of all energy levels towards higher values (see before). This implies a larger hybridization between the states of the atomic species and the Fe states below the Fermi levels leading to a stronger interaction between adsorbed atoms and surface and a larger binding energy, more evident for S than for H species. This occurs passing from (100) to (310) for H and vice-versa for the S species.

It might be surprising to find a smaller adsorption strength for S on the stepped surface, given the same adsorption site. See Tables 3.1 and 3.2). But we remark that the Fe(310) stepped surface does not display a terrace, since the steps are too close to one another. In particular, the ($4h$) site of the (100) facets of the (310) surface (see Fig. 1b) is a hollow site adjacent to step edges both from below (where adsorption is commonly stabilized) and from above (where instead a weaker bonding may be expected) so that the net result is not easily predictable from common sense. The comparison to other adsorbates is to be done, to this respect, always considering adsorption in four-fold hollow sites: indeed, in this case, also HS and H_2S are less bonded to the surface (H_2S is not even stable in 4h sites of Fe(310) than in hollow sites of Fe(100)). The only exception here is H, which is 0.04 eV more stable at the (310) surface. In conclusion, the step edge offers reactive bridge sites which

are energetically more convenient for HS and H_2S but not for S. We also wish to add that the hollow site involves Fe atoms with different coordination on the two surfaces. On Fe(100), all Fe atoms have 4 NN, while on Fe(310) two have 6 NN and the other two have 4 NN (even though the number of second neighbors is lower than that on the flat surface). Apparently, the Fe atoms at this stepped surface are on the average more coordinated than on the flat one, hence justifying the weaker binding found.

3.2.2 HS Adsorption on Fe(310)

The HS ion on Fe(310) changes its preferred site with respect to that on the (100) surface. In fact a bridge site (b_2) represents the deeper minimum for the (310) surface rather than a hollow one, with an adsorption energy equal to of -3.29 eV, slightly larger than that in the hollow site of Fe(100) (-3.35 eV). The H-S bond length (1.361Å) is about the same as in the gas phase (whose calculated value is 1.398 Å). The HS ion lies almost parallel to the terraces of the surface with an angle of 79.8° with respect to the surface normal. The optimized configuration is depicted in panel (a) of Fig. 3.5. As we found for S, the hollow site is more stable on the flat surface rather than on the stepped one. However, the bridge site involves only Fe atoms at the step edge and is stabilized (as expected) by 0.16 eV on Fe(310), eventually becoming the preferred adsorption site for this surface.

Figure 3.6 shows the LDOS of HS projected onto the s and p states of the H and S atoms, for adsorption at the bridge site on Fe(100) (chosen for its larger similarity to the stepped surface one) in panel (a), and the same LDOS at the (b_2) site for Fe(310), in panel (b). The energy positions of s and p states involved in the S-H bonding is about the same for both surfaces. However, a small shift to lower energies of the s-p projected LDOS

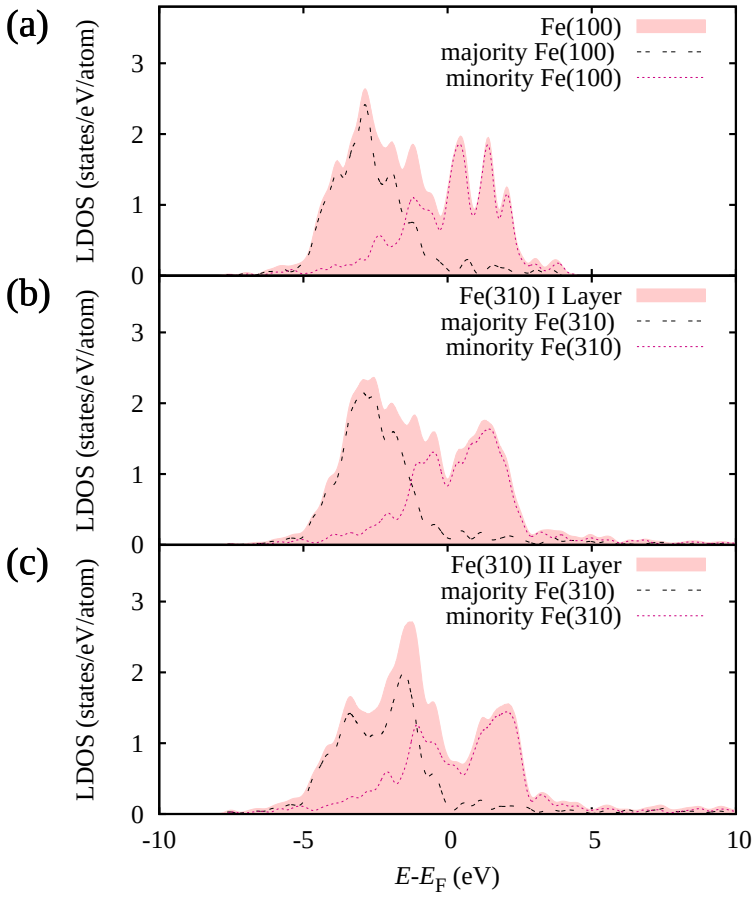

Figure 3.2: *Comparison between the LDOS of the outermost Fe atoms of the clean surfaces. Panel (a), first layer of Fe(100); panel (b), first layer of Fe(310); panel (c) second layer of Fe(310). Majority and minority spin contributions are shown.*

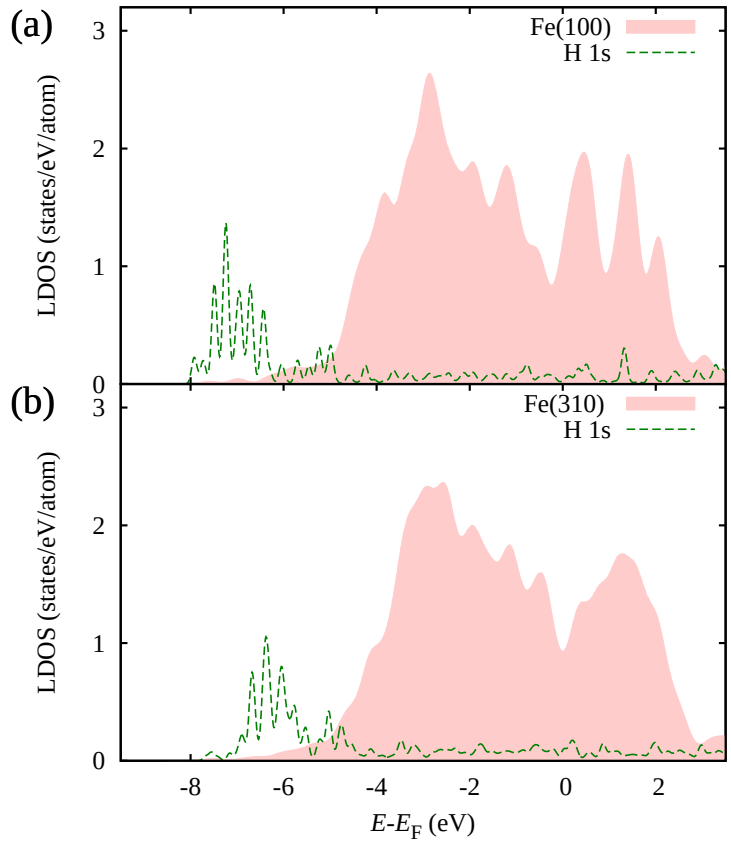

Figure 3.3: *Comparison between the LDOS for H adsorption on Fe(100), panel (a), and Fe(310), panel (b). For the shaded area see the text.*

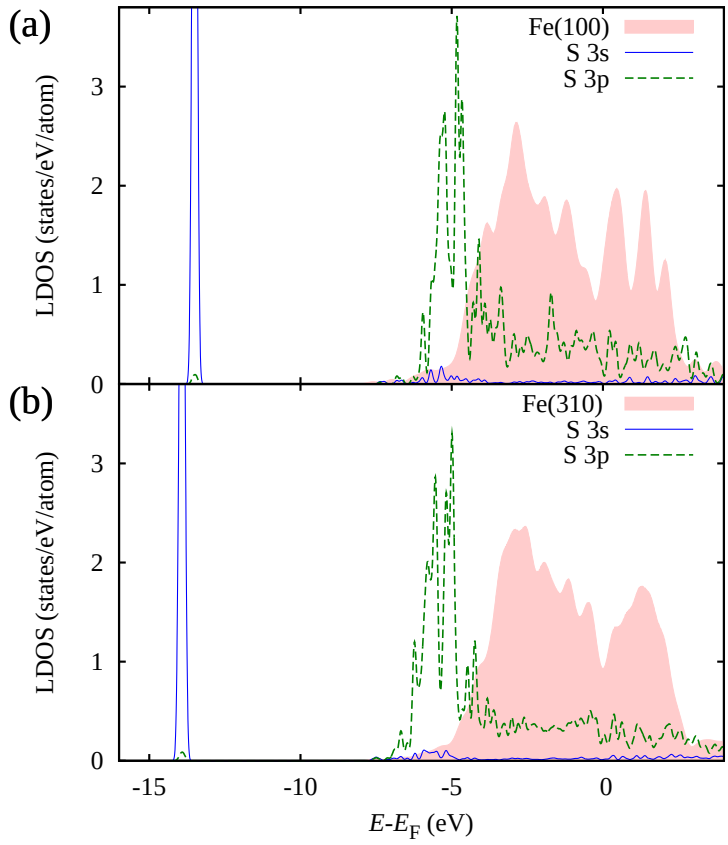

Figure 3.4: *Comparison between the LDOS for S adsorption on Fe(100), panel (a), and Fe(310), panel (b). Shaded area as in Figure 3.*

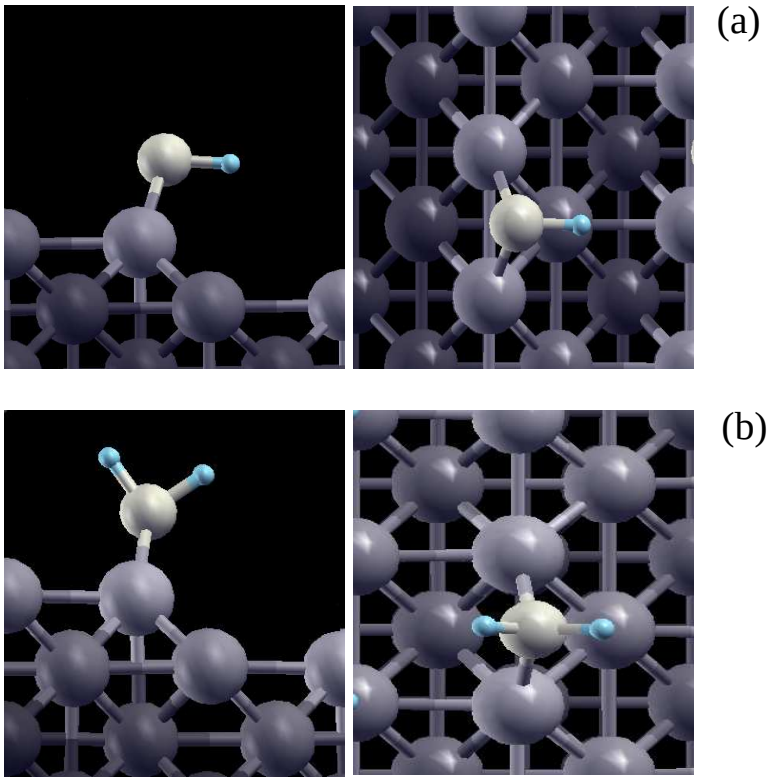

Figure 3.5: *Side and top view of the adsorption configuration in the most stable (b_2) site for HS, panel (a), and H_2S, panel (b).*

for HS/Fe(310) is observed signaling a slightly weaker bond than on Fe(100). In both cases, the deeper peak is composed mainly by the s states of S and H. The next one is composed by the s state of H and mainly by the S p-states in the y direction perpendicular to the step edge and to the surface normal (z), with a smaller component of the p_z state. The broad band which appears at larger energies is instead due mainly to the p_x orbital (parallel to the step edge) and to some extent to the p_z one, and is significantly hybridized with the Fe states. These states are responsible for the HS-surface binding and are narrower and centered at lower energies in the Fe(310) case.

3.2.3 H_2S Adsorption on Fe(310)

In panel (b) of Figure 3.5, the most stable high-symmetry site for adsorption of H_2S on Fe(310), i.e. (b_2), is depicted. This configuration presents a weak adsorption energy of -0.45 eV, while (b_1) and ($3h_1$) are even less stable both at an energy of -0.24 eV. Nevertheless, there is a weak increasing in the binding energy of H_2S on Fe(310) with respect to that on Fe(100) (-0.39 eV at the most stable bridge site). In (b_2) the molecule lies in a plane perpendicular to the step edges, with the two H atoms pointing out of the surface. In the same site, other orientations of the molecule were simulated but proven to be unstable, or leading to dissociation of the molecule without any barrier when H_2S was placed close to the surface in structural optimizations, in line with easy dissociation of molecular hydrogen sulphide on the iron surface. With regard to the geometry, both for Fe(100) and Fe(310) adsorption, there is only a slight change in bond length and in the HSH angle with respect to that of H_2S in gas phase, whose calculated values are 1.352 Å and 91.1°, respectively. These small changes are consistent with the weak interaction between molecular H_2S and the surface (see Tab. 3.2).

Figure 3.7 shows the comparison between the total projected LDOS onto the s and p states of H and S atoms of the H_2S molecule, in the case of adsorption on Fe(100), panel (a), and Fe(310), panel (b). The calculated energies of the molecular orbitals up to LUMO are also reported by arrows in Fig. 3.7, with energy reference chosen to align the lowest level to the same one for H_2S/Fe(100). From Tables 3.1 and 3.2 we note that there is a very small difference in binding energy between the two surfaces (0.06 eV larger on Fe(310)). In Fig. 3.7 first, from both panels (a) and (b), one can distinguish the s states of the S atom hybridized with the s ones of H (the deepest peak). This could be associated to the $1a_1$ bonding orbital of H_2S, that does not interact with the surface.

Moving towards the Fermi level the p band of the S atom is found. The deeper peaks, composed by the p_y and p_z projections (perpendicular to the step edge and x axis) are also hybridized with the s states of the H atoms. They can be associate with $1b_2$ and $2a_1$ molecular orbitals and are also responsible for H-S bonding. The following structure derives from the lone pair of the molecule, i.e., the HOMO b_1, which is mostly composed by the p_x states of sulfur. This is responsible for the interaction with the surfaces and appears very similar for Fe(100) and Fe(310). In conclusion, the LDOS's of H_2S on the two surfaces display smaller differences, as compared to the species reported before, due to a smaller adsorbate-surface interaction.

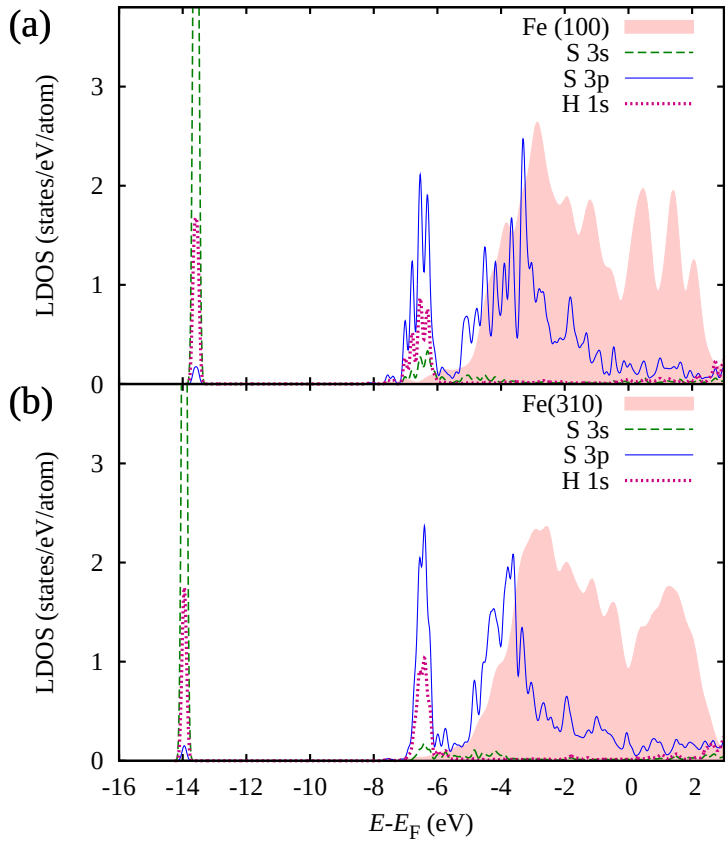

Figure 3.6: *Comparison between the LDOS for HS adsorption on Fe(100), panel (a), and Fe(310), panel (b). Shaded area as in Figure 3.2.*

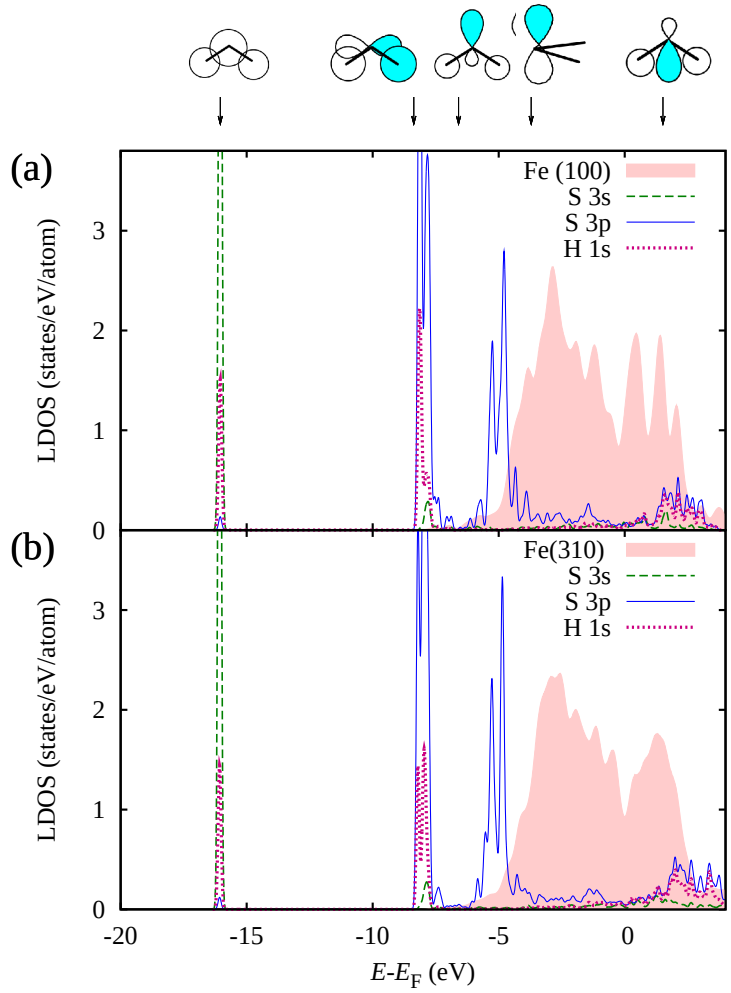

Figure 3.7: *Comparison between the LDOS for H_2S adsorption on Fe(100), panel (a), and Fe(310), panel (b). Shaded area as in 3.2. Arrows denote molecular orbital energies in the free molecule.*

Conclusions

In the framework of periodic density functional theory, we studied H_2S, HS, H and S adsorption on a stepped (310) iron surface at $\theta = 0.30$ ML coverage, comparing our results with those previously obtained for the same species in the case of Fe(100).

We find that for S and HS a strong binding is still predicted, but with slightly smaller adsorption values on Fe(310) than on Fe(100). Conversely H and H_2S are more strongly adsorbed on the stepped surface than on the Fe(100) one. Both H and HS occupy different stable configurations on Fe(310) with respect to the ones on Fe(100) (hollow in both cases), namely a three-fold hollow site for H and the bridge one at the step edge for HS. On the contrary, adsorption of S and H_2S occurs in the same high-symmetry sites on Fe(310) as on Fe(100), namely the four-fold hollow site for S and a bridge one (at the step edge) for H_2S. Different coordination numbers of Fe atoms involved in the four-fold hollow site for Fe(310), with apparently increased average coordination, may account for the reduced adsorption energy of most species in this site with respect to the same one on Fe(100). This is not a general result, but it follows for the particular shape of the stepped surface.

The analysis of the calculated LDOS is useful to remark and confirm common trends with adsorption energies. In particular, a stronger binding

is predicted when there is a decrease in the relative distance between the atom's orbital and the weighed average energy of the projected d bands of the metals. Indeed this occurs for H and H_2S on Fe(310) and S and HS on Fe(100).

List of Figures in Part I

List of Tables in Part I

Bibliography

[1] Acet M., Zahers H., Wassermann E.F., Pepperhoff W., Phys. Rev. B **49**, (1994) 6012. 26

[2] Alfonso D.R., Surf. Sci. **602**, (2008) 2758. 4

[3] Armiento R. and Mattsson A.E., Phys. Rev. B **72**, (2005) 085108.

[4] Ashcroft N. W. and Mermin N. D., *Solid State Physics*, Saunders College Publishing, Texas (1985). 16

[5] Blyth R.I.R, et al., Phys. Rev. B **68**, (2003) 205404. 8, 16

3

[6] Boski P. and Kiejna A., Surf. Sci. **601**, (2007) 123. 4

[7] Briant C.L., Sieradzki K., Phys. Rev. Lett. **63**, (1989) 2156. 3

[8] Brivio G.P., Trioni M.I., Rev. Mod. Phys **71**, (1999) 231. 5, 29, 31

[9] Campbell C.T., Koel B.E., Surf. Sci. **183**, (1987) 100. 3

[10] Dreizler M.R. and Gross E.K.U., *Density Functional Theory : An Approach to the Quantum Many-Body Problem*, Springer, Berlin, (1990). 10

[11] Feynman R.P., Phys. Rev. **56**, (1939) 340. 9

[12] Geerlings P., Proft F.D., and Langenaeker W., Chem. Rev., **103**, (2003) 1793. 10

[13] Giannozzi P., et al., J. Phys. Condens. Matter **21**, (2009) 395502. 25

[14] Hamann D.R., Schlu̇ter M. and Chiang C., Phys. Rev. Lett. **43**, (1979) 1494. 18

[15] Hammer B., Nørskov J.K., Surf. Sci. **343**, (1995) 211. 21, 28, 29, 31

[16] Hammer B., Nørskov J.K., "Chemisorption and Reactivity on Supported Clusters and Thin Films", R.M. Lambert and G. Pacchioni, NATO ASI Series E No. 331 (Kluwer Academic Dordrecht), (1997). 21, 31

[17] Hammer B., Hansen L.B., and Nørskov J.K., Phys. Rev. B **59**, (1999) 7413. 15

[18] Hammer B., Nørskov J.K., Advances in Catalysis **45**, (2000) 7. 5, 21, 29

[19] Hedge R.I, White J.M, J. Phys. Chem **90**, (1986) 296. 3

[20] Hohenberg P., Kohn W., Phys. Rev **136**, (1964) B864. 10, 25

[21] Inglesfield J., Prog. Surface Sci. **20**, (1985) 105. 20

[22] Jaffey D.M., Madix R.J., Surf. Sci **314**, (1991) 23. 3

[23] Jiang D.E., Carter E.A., Phys. Rew. B **70**, (2004) 064102. 30, 47

[24] Jiang D.E., E.A. Carter E.A., J. Phys. Chem. B **108**, (2004) 19140. 4

[25] Jiang D.E., E.A. Carter E.A., J. Phys. Chem. B **109**, (2005) 20469. 4, 29, 30, 47

[26] Jiang D.E., E.A. Carter E.A., Surf. Sci. **60**, (2009) 583. 4

[27] Johnson S., and Madix R.J., Surf. Sci. **108**, (1981) 77. 3

[28] Jones R. O. and Gunnarsson O., Rev. Mod. Phys. **61**, (1989) 689. 10

[29] Koestner R.J., et. al., Chem. Phys. Lett. **125**, (1986) 134. 3

[30] Kohn W., Sham L., J. Phys. Rev **140**, (1965) A1133. 10, 12, 25

[31] Kose R., Brown W.A., and King D.A., J. Am. Chem. Soc. **121**, (1999) 4845. 4

[32] Leavit A.J., Beebejr T.P., Surf. Sci. **314**, (1994) 23. 3

[33] Martin R.M., *Electronic Structure, Basic Theory and Practical Methods*, Cambridge University Press, (2004). 17

[34] Masel R., *Principles of Adsorption and Reaction on Solid Surfaces*, Wiley Series in Chemical Engineering (1996). 20

[35] Mattsson A.E., Armiento R., Paier J., Kresse G., Wills J.M., and Mattsson T.R., J. Chem. Phys. **128**, (2008) 084714. 16

[36] Monkhorst H.J. and Pack J.D., Phys. Rev. B **13**, (1976) 5188. 17

[37] Narayan P.B.V., Anderegg J.W., Chen C.W.J., J. Electron Spectrosc. Relat. Phenom **27**, (1982) 233. 4

[38] Nielsen O.H. and Martin R.M., Phys. Rev. Lett. **50**, (1983) 697. 9

[39] Parr R.G. and Yang W., *Density Functional Theory of Atoms and Molecules*, Oxford University Press, New York, (1989). 10

[40] Perdew J.P., Bruke K., Ernzerhof M., Phys Rev. Lett. **77**, (1996) 3865. 15, 25

[41] Perdew J.P., Burke K., and Wang Y., Phys. Rev. B **54**, (1992) 16533. 15

[42] Perdew J.P., Ruzsinszky A., Csonka G.I., Vydrov O.A., Scuseria G.E., Constantin L.A., Zhou X., and Burke K., Phys. Rev. Lett. **100**, (2008) 136406. 15

[43] Perdew J.P. and Schmidt K., *Density Functional Theory and Its Application to Materials*, V. Van Doren, AIP Press, Melville, New York, (2001). 14, 15

[44] Ramsier R.D., Gao Q., Neergaard Walterburg H. and Yates J.T, J. Chem. Phys. **100**, (1994) 6837. 4

[45] Rice J., Wang J.S., Mater. Sci. Eng. A **107**, (1989) 23. 3

[46] Rovida G., Pratesi P., Surf. Sci. **104**, (1981) 609. 3

[47] Scheffler M., and Stampfl C., *Theory of Adsorption on Metal Substrates, Handbook of Surface Science*, Vol 2,Horn K. and Scheffler M. (2000). 20, 22

[48] Srihrishnam V., Liu H.W., Ficalora P.J., Scr. Metall. **9**, (1975) 1341. 3

[49] Vitos L., Ruban A.V., Skriver H.L., Kollár J., Surf. Sci. **411**, (1998) 186. 4, 5

[50] Warren E. Pickett, Computer Physics Report **9**, (1989) 115. 18

[51] Wilke S. and Scheffler M., Surf. Sci. **329**, (1995) L605. 3

[52] Wu Z. and Cohen R.E., Phys. Rev. B **73**, (2006) 235116.15

[53] Yu Y., Dixon-Warren St.J., Astle, N., Chem. Phys. Lett. **312**, (1999) 455. 3

[54] Zhang Y. and Yang W., Phys. Rev. Lett. **80**, (1998) 890. 15

[55] Ziegler T., Chem. Rev. **91**, (1991) 651. 10

Part

Scattering wave packets generated at a finite distance

Introduction

The recent developments of nanotechnology and the advent of modern high-speed high-density MOS devices, have revived the technological and theoretical interest of the scientific community in the tunneling problem, since they require extremely short channel lengths for improving performance and decreasing size. The development of ultrascaled nanometric CMOS compatible single electron transistors (SETs) and single atom trasistors [25, 34] has lead, together with sequential tunneling of single/few electrons regime, the emergence of density of states graining and fluctuations in the contacts [8, 24]. Confinement effects in the contacts may determine discretization of energy levels, charge localization at intradopant length scale, valley orbital splitting [33], and selection rules on quantum states in tunnelling. Consequently, the understanding of dependence of tunneling across a barrier from the position constitutes a relevant aspect in view of Beyond CMOS and More Moore technology developments.

The large relevance of such quantum effects on micro devices has also revived the theoretic interest in the well known problem of the tunneling time, i.e. the time spent by the particle to tunnel through the barrier [16, 28, 35, 7, 37, 41, 23, 50, 12, 31], insomuch as numerous works were published on this subject over the last ten years [15, 36, 52, 49]. Surprisingly, no answer to such

a question has been definitively accepted yet despite the fact that a variety of definitions of tunneling time have been proposed. We emphasise that, in most of these approaches, while the particle is described as a wave packet, its energy is assumed to be an assigned value so that its dispersion, which may play a fundamental role in several dynamical situations, is completely ignored.

In this work we point out that, in real cases, only a wave packet approach can adequately describe the dynamics of a particle. In fact, the stationary plane wave picture, usually adopted as an approximated scheme for standard analysis of such problems, intrinsically neglects the initial conditions of the wave packet in terms of its origin $x(0)$ and spread $\sigma_x(0)$, which conversely play, as we will show, an important role in such an analysis. We concentrate our attention on the dynamics of a Gaussian wave packet (GWP) scattering on a step potential. To solve the Schrödinger equation, we have implemented a code, based on a Crank-Nicholson finite difference scheme with absorbing boundary conditions, to emulate the wave packet propagation to infinity. Our code works in 3-d, with any number and shape of barriers. Through a numerical solution of the Schrödinger equation we analyse the evolution of the system calculating the transmission of the scattering GWP as a function of the initial $\sigma_x(0)$ and $x(0)$ conditions, and comparing simulated data with theoretical results.

Further important issue about scattering emerges by the numerical analysis on the probability of the system to cross the barrier as a function of time t, which seems to be neglected by literature to the best of our knowledge. Namely, how much time after the scattering event the wave packet spends to reach the asymptotic regime, in which the particle has achieved its asymptotic probability to be observed beyond the barrier. Of course, since the

support of a Gaussian is not compact, the interactions with the potential are ever-present and, in principle, this time is not finite. However, for all practical purposes, we define a finite time which accounts, within the confidence limits, for a fixed amount (namely 0.99) of the normalized probability of the transmitted wave packet. We name this time interval the *formation time* t_{f}. Numerical results show that t_{f} strongly depends on x_0. To analytically express such a dependence, we propose a semi-classical approximated model in which t_{f} is described as the time spent by a finite support (accounting for the 0.99 of the probability) of the incident wave packet to cross the barrier, namely the time required to locate, in coordinate space, the greatest amount of the GWP's probability distribution beyond the barrier interface. This could be a relevant aspect, mainly in solid state physics, in those phenomena, of large conceptual and practical interest, which are characterized by incoming particles generated by scattering centres at a *finite* and *randomly distributed* distance from surface.

- Chapter 1 -

Dynamics of interacting Gaussian wave packet

This chapter is dedicated to a general overview of the quantum mechanical description of a particle and its dynamics with relation to the scattering process. After a discussion about the importance to describe the quantum particle in a wave packet frame , we focus on the Gaussian wave packet dynamics for the free motion and in the case of 1-d scattering.

§ 1.1 Particle as a wave packet

The interaction of a particle in a box with a potential barrier is generally achieved by describing the particle in terms of monochromatic waves [2, 10, 40, 22, 26, 51].

However, we note that there are a variety of phenomena, mainly in solid state physics, in which the incoming particles are generated by scattering centres at a *finite* distance from the potential barrier. We refer, for example, to the following scenarios: the passage of hot electrons from the channel

to the floating gate, in non-volatile memories, during the writing cycle; the Fowler–Nordheim tunneling [11] of trapped electrons during the erase of the information stored in floating gate; the filtering of hot electrons by defects, in thermoelectricity. In the above contexts, it is especially interesting to observe that the entire treatment of the problem of scattering at the surface, in terms of energy eigenstate, is manifestly difficult and any description of such phenomena in terms of stationary plane waves is inadequate. On the other hand, they are easily framed in the wave packet description, simply assuming that the scattering centres generating the wave packet are localized. If these centres are of atomic nature, the maximum information one can provide on the origin of the particle is a distribution of atomic size (say 0.2–0.4 nm), whereas if they are attributed to lattice imperfections the particle is localized with an uncertainty typically of the order of 5 nm. For the above phenomena, the spread resulting from the localization condition is not negligible with respect to the mean free path (for electrons in solids $\lambda \approx 10$ nm)—that renders especially difficult the disentanglement of phenomena due to the initial wave packet spread and mean free path.

More generally, the description of a particle in a non-stationary state as a wave packet (usually a GWP) has striking advantages. *First* of all, the wave packet description provides a detailed knowledge of the wave function evolution approaching the step potential, and it is able to provide a measure of the time required to form the escaping and backscattered wave functions as a function of particle dynamical properties (mean kinetic energy, energy dispersion) and of its original position and space dispersion. *Second*, while the description in terms of stationary waves can be applied to physically interesting problems only for potentials subject to very restrictive conditions, the use of GWP can be applied to potentials which vary even in a non-

monotonic way with x. In the last case, the major difficulties come from the fact that a wave packet, initially Gaussian, remains so only for quadratic, linear, or constant potentials and that, in general, a non-Gaussian packet does not preserve the norm [14]. *Third*, the use of GWP allows an easy interpretation in semi-classical terms. Just like the free motion of a classical particle with momentum p is frictionless occurring with velocity v, given by $v = p/m$, the free motion of the GWP with mean wave number $\langle k \rangle$ is frictionless and occurs with a group velocity $v_{\rm g}$ given by $v_{\rm g} = \hbar\langle k \rangle/m$ (the classical velocity).

The major differences between the classical and wave packet description of the particle are that

- in classical mechanics a particle in a definite energy state is able to drift whereas in quantum mechanics that would be impossible (the space probability distributions for eigenstates of energy are stationary);
- the analogy is possible only by exchanging the quantum mechanical expectation values with the corresponding classical values, and better the sharper are the quantum mechanical distributions are.
- the quantum mechanical nature of the particle does anyway emerge because of the almost linear asymptotic increase with time t of the spread of the wave packet, in agreement with the general behaviour of the spread of the wave function.

Despite the fact that wave packet approach offers the above advantages, some of the aspects connected with the wave packet dynamics remain controversial. We refers, for example, to the dependence of the phase and delay time on the distance between the wave packet origin x_0 and the barrier , or the acceleration of the transmitted wave packet by an opaque potential

barrier [16, 23]. Moreover, within the context of the non-stationary scheme, two problems seem physically interesting. First of all, the description of the evolution of the original GWP into two non-overlapping wave packets, as a function of the initial position, and in particular the characteristic time spent by the system to reach the above condition. As we will see in the next session, we define it, within some approximations, as the *formation time* t_{f}. Second, the relation between such a time and the underlying energetics (energy and energy dispersion) of the impinging particle and of the newly formed particles. For these kind of problems, literature is mainly focused on the potential barrier (rather than on the step) looking at estimating the *tunneling time*, i.e. the time spent by the particle to tunnel through the barrier [15, 36, 52, 49]. We stress that in most of these approaches while the particle is imagined as a wave packet, it is assumed to be in an assigned energy value so that its dispersion is totally ignored.

In the next sections, we will concentrate our attention on the above two problems, proposing a semi-classical model, to study the dynamics of the wave packet impinging a potential step and comparing it with numerical results. As we will see, our approach picks out the relevance of the energy spread and of the initial condition x_0 on the behaviour of the system. Manifestly, these quantities are not considered in any treatment of the problem where the particle is initially in an energy eigenstate.

§ 1.2 Dynamics of a free Gaussian wave packet

In this section we briefly review free motion of a quantum particle, and then focus our attention on the step potential as a benchmark case for the scattering process.

As it is well known, the dynamics of a quantum particle of mass m moving in one dimension, along the coordinate x, with Hamiltonian H, and potential $V(x)$ is ruled by the following time dependent Schrödinger equation(TDSE):

$$i\hbar\frac{\partial\Psi(x,t)}{\partial t} = \left(H^0 + V(x)\right)\Psi(x,t) = -\frac{\hbar^2}{2m}\frac{\partial^2\Psi(x,t)}{\partial x^2} + V(x)\Psi(x,t) \quad (1.1)$$

where t is time, $\hbar$ is the Planck's constant, and the solution $\Psi(x,t)$ is normalized to unity:

$$\int \mid \Psi(x,t) \mid^2 \mathrm{d}x = 1. \quad (1.2)$$

It can be shown that the more general solution of equation (1.1), complying with the superposition principle, can assume the following form:

$$\Psi(x,t) = \int \Phi(k,t)e^{ikx}\mathrm{d}k. \quad (1.3)$$

where $\Phi(k,t)$ is the envelope function, in general complex, e^{ikx} are the eigenfunctions (plane-waves MWs) of momentum operator P and k is the wave number such that for the eigenvalues p holds: $p = \hbar k$.

The function $\Psi(x,t)$ is called *wave packet* (WP). Note that, it is nothing but the Fourier transformation of $\Phi(k,t)$, that is the wave packet in momentum representation.

Also for practical purpose, the Gaussian envelope $\Phi(k,t)$ (GWP) is usually chosen, first because it is analytically manageable, and then because it verifies the Heisenberg uncertainty principle, as we will see later.

In the case of free particle we can rewrite $\Phi(k,t)$ as

$$\Phi(k,t) = \Phi(k,0)e^{-i\omega(k)t} \quad (1.4)$$

where the phase $\omega(k)$ is the De Broglie's dispersion relation for energy $E = \frac{\hbar^2k^2}{2m}$.

The more general Gaussian free wave packet, with arbitrary initial values for position x_0, momentum k_0 and spread σ_k, can be written in momentum space as

$$\Phi(k,0) = \left(\frac{1}{2\pi\sigma_k^2}\right)^{1/4} e^{\frac{-(k-k_0)^2}{4\sigma_k^2}} e^{-ikx_0} \tag{1.5}$$

Substituting (1.4) and (1.5) in (1.3) and performing the integrations, one obtains:

$$\Psi(x,0) = \left(\frac{1}{2\pi\sigma_x^2(0)}\right)^{1/4} e^{\frac{-(x-x_0)^2}{4\sigma_x^2(0)}} e^{+ik_0(x-x_0)} \mathrm{d}k. \tag{1.6}$$

This is also a Gaussian packet with the spread $\sigma_x(0)$ which, due to the Heisenberg uncertainty principle, results:

$$\sigma_x(0) = \frac{1}{2\sigma_k(0)}. \tag{1.7}$$

With the same procedure as above, the evolution of the GWP $\Psi(x,t)$ can be deduced:

$$\Psi(x,t) = \left(\frac{8\sigma_x^2(0)}{\pi}\right)^{1/4} \frac{e^{i\phi}}{\left[(2\sigma_x(0))^4 + \frac{4\hbar^2t^2}{m^2}\right]^{1/4}} \exp\left[-\frac{\left(x - \frac{\hbar k_0}{m}t\right)^2}{(2\sigma_x^2(0))^2 + \frac{2i\hbar t}{m}}\right] e^{-ikx_0} \mathrm{d}k. \tag{1.8}$$

where $\phi = -1/2 \arctan(\frac{2\hbar t}{4\sigma_x^2(0)m}) - \frac{\hbar k_0^2}{2m}t$

with the following position-space probability density:

$$|\Psi(x,t)|^2 = \left(\frac{1}{2\pi\sigma_x^2(0) + \frac{\hbar^2t^2}{4m\sigma_x^2(0)}}\right)^{1/2} \exp\left[-\frac{\left(x - \frac{\hbar k_0}{m}t\right)^2}{2\left(\sigma_x^2(0) + \frac{\hbar^2t^2}{4m\sigma_x^2(0)}\right)}\right] \tag{1.9}$$

The Fourier transformation of (1.8) defines the evolution of a Gaussian $\Phi(k,t)$ in the momentum representation:

$$\Phi(k,t) = \int \Psi(x,t) \mathrm{e}^{-ikx} \mathrm{d}x \tag{1.10}$$

Also in this case, performing the above integral one obtains the explicit expression of the GWP as a function of time (as follows from (1.5) and (1.4)),

$$\Phi(k,t) = \left(\frac{1}{2\pi\sigma_k^2}\right)^{1/4} e^{\frac{-(k-k_0)^2}{4\sigma_k^2}} e^{-ikx_0} e^{-i\omega(k)t} \tag{1.11}$$

with probability density:

$$|\Phi(k,t)|^2 = |\Phi(k,0)|^2 \tag{1.12}$$

We use the quantum mechanics standard notation for the evaluation of the mean value of an operator $A(\alpha)$ as a function of a continuous variable α

$$\langle A(\alpha)\rangle = \int \Psi(\alpha)^* A(\alpha)\Psi(\alpha)\mathrm{d}x \tag{1.13}$$

In the case of free particle applying (1.13) to (1.11) and (1.8) the following equations hold:

$$\begin{aligned} \langle x(t)\rangle &= x_0 + \tfrac{\hbar k_0 t}{m} \\ \sigma_x(t)^2 &= \sigma_x(0)^2 + \tfrac{\hbar^2 t^2}{4m^2\sigma_x(0)^2} \\ \langle k(t)\rangle &= k_0 \\ \sigma_k(t) &= \tfrac{1}{2\sigma_x(0)} \end{aligned} \tag{1.14}$$

As we can see from (1.9),(1.12) and from the (1.14), in coordinate representation, the free GWP's center $x_0(t)$ moves with constant velocity and spreads following the second of (1.14). On the other hand, in momentum representation the GWP and its square modulus remains constant.

§ 1.3 Scattering Theory

As we want to study the dynamics of the GWP and its dependence by the initial conditions x_0 and spread $\sigma_x(0)$, we concentrate our attention on the problem of the scattering of a GWP by a step potential, reducing for simplicity in 1-d space.

In this section, first we provide a general setting of the scheme used to describe the dynamics of the scattering [44] and then we provide the

interesting physical quantities and properties in the particular case of a step potential, which will be the subject of our analysis in the next sessions.

1.3.1 1-d Scattering Theory

The general equation (1.1) can assume the form

$$\psi(x,t) = U(t,t_0)\psi(x,t_0) \tag{1.15}$$

where the unitary operator $U(t,t_0) \equiv e^{-iH(t-t_0)/\hbar}$ is called the evolution operator. In this way a wave function representing the evolution of a particle at time t can be uniquely identified by an initial wave function $\psi(x,t_0)$ at time $t = t_0$.

Now we consider a scattering process where $\psi(x,t)$ represents the evolution of the scattering particle, it means that the backward time propagation of $\psi(x,t)$ is described by a free wave packet very far from the scattering region (asymptotic region). But the evolution on time of a free wave packet ($\psi_{\text{in}}(x,t)$) is described by the following equation:

$$\psi_{\text{in}}(x,t) = U^0(t,t_0)\psi_{\text{in}}(x,t_0) = e^{-iH^0(t-t_0)/\hbar}\psi_{\text{in}}(x,t_0) \tag{1.16}$$

Hence the following relation is established:

$$\lim_{t\to-\infty} U(t,t_0)\psi(x,t_0) - U^0(t,t_0)\psi_{\text{in}}(x,t_0) = 0 \tag{1.17}$$

it means that very far in time, before the scattering, the dynamical behaviour of $\psi(x,t)$ is undistinguishable from a free packet.

In the same manner, the evolution in the future $\psi_{\text{out}}(x,t)$ of the scattered state very after the scattering event and far from the scattering region, can be deduced by a similar relation:

$$\lim_{t\to+\infty} U(t,t_0)\psi(x,t_0) - U^0(t,t_0)\psi_{\text{out}}(x,t_0) = 0 \tag{1.18}$$

.

Equations (1.17) and (1.18) define respectively the incoming asymptotic state ("in" state) $\psi_{\text{in}}(x, t_0)$ and the outgoing asymptotic state ("out" state) $\psi_{\text{out}}(x, 0)$, of the interacting system.

From previous relation (1.17) and (1.17), it is clear that

$$\begin{aligned} \psi(x, t_0) &= \lim_{t \to -\infty} U(t, t_0)^\dagger U^0(t, t_0) \psi_{\text{in}}(x, t_0) \\ \psi(x, t_0) &= \lim_{t \to +\infty} U(t, t_0)^\dagger U^0(t, t_0) \psi_{\text{out}}(x, t_0) \end{aligned} \tag{1.19}$$

.

Finally defining the operators $\Omega_\pm$ as

$$\Omega_\pm = \lim_{t \to \pm\infty} U(t, t_0)^\dagger U^0(t, t_0) \tag{1.20}$$

it is possible to establish the following relation

$$\psi_{out}(x, 0) = \Omega_+ \Omega_- \psi_{in}(x, t_0) = S \psi_{in}(x, t_0) \tag{1.21}$$

.

This defines the unitary Scattering operator $S = \Omega_+ \Omega_-$, which will be useful in the next section

1.3.2 The potential Step

In order to evaluate the role of initial condition on the dynamics of the scattering process, it means how the initial wave packet center x_0 and width $\sigma_x(0)$ modifies the evolution of $\psi_{in}(x, t_0)$ toward $\psi_{out}(x, t_0)$, we concentrate our attention on the problem of scattering by a potential step, so avoiding tunneling contribute.

In this case the Hamiltonian in (1.1) contains a potential of the form:

$$V(x) = \begin{cases} 0 & \text{for} \quad x \in \mathcal{D}_x^- \\ V_{\mathrm{B}} & \text{for} \quad x \in \mathcal{D}_x^+ \end{cases} \tag{1.22}$$

where $\mathcal{D}_x^- =]-\infty, x_{\mathrm{B}}[$, $\mathcal{D}_x^+ = [x_{\mathrm{B}} + \infty[$, x_{B} is the discontinuity point, and V_{B} is the potential height.

Standard analysis of scattering [2, 26, 51, 3] of a particle impinging on a potential $V(x)$ is usually described in the stationary framework, which is based on the following assumptions:

- the initial asymptotic state of the particle $\psi_{in}(x, t_0)$ is described by a stationary state, simultaneously eigenfunctions of energy and momentum, represented by the plane waves (MWs):

$$\psi_{in}(x, t_0) = \varphi_{(\pm k)}(x) = (2\pi)^{-1/2} \mathrm{e}^{\pm ikx} \tag{1.23}$$

- States with positive momentum describe a forward motion, representing the transmitted channel.

- States with negative momentum describe a backward motion , representing the reflected channel.

- The physical situation of an incoming particle undergoing scattering is accounted imposing that for the backward solution is nil in the region beyond the scattering region.

- The potential V_{B} separates the scattering region, and hence the support of the solution $\psi(x, t_0)$, in two disconnected domains where the Hamiltonian of the system commutes with the momentum operator, separately.

- The left side $\mathcal{D}_x^-$ of the barrier, contains the linear superposition of the two (incident and reflected) MWs, while the complementary $\mathcal{D}_x^+$ contains only the transmitted MW.

$$\psi_{\rm out}(x) = \begin{cases} \varphi_{(+k')}(x) + r(k',k'')\varphi_{(-k')}(x) & \text{for} \quad x \in \mathcal{D}_x^- \\ t(k',k'')\varphi_{(+k'')}(x) & \text{for} \quad x \in \mathcal{D}_x^+. \end{cases} \tag{1.24}$$

where

$$k = \begin{cases} k' = \pm\sqrt{2mE/\hbar^2} & \text{for} \quad x \in \mathcal{D}_x^- \\ k'' = \sqrt{2m(E-V_{\rm B})/\hbar^2} & \text{for} \quad x \in \mathcal{D}_x^+ \end{cases} \tag{1.25}$$

$$k'' = \pm\sqrt{k'^2 - 2mV_{\rm B}/\hbar^2} \tag{1.26}$$

and $r(k',k'')$ and $t(k',k'')$ are obtained solving the Schrödinger equation separately in the different regions and imposing continuity boundary conditions for the wave function and its derivative

$$t(k',k'') = \frac{2k'}{k'+k''} = \frac{2\sqrt{(E(k)-V_{\rm B})}}{\sqrt{E(k)}+\sqrt{(E(k)-V_{\rm B}}} \tag{1.27}$$

$$r(k',k'') = = \frac{k'-k''}{k'+k''} = \frac{\sqrt{E(k)}+\sqrt{(E(k)-V_{\rm B})}}{\sqrt{E(k)}-\sqrt{(E(k)-V_{\rm B}}} \tag{1.28}$$

Finally the solution can be rewritten as:

$$\psi_{\rm out}(x) = \left[\psi_{\rm in}^{\rm I}(x) + \psi_{\rm out}^{\rm R}(x)\right]\Theta(x_{\rm B}-x) + \psi_{\rm out}^{\rm T}(x)\Theta(x-x_{\rm B}) \tag{1.29}$$

where:

$$\begin{aligned} \psi_{\rm in}^{\rm I}(x) &= \varphi_{(+k')}(x) \\ \psi_{\rm out}^{\rm T}(x) &= t(k)\varphi_{(+k'')}(x) \\ \psi_{\rm out}^{\rm R}(x) &= r(k)\varphi_{(-k')}(x) \end{aligned} \tag{1.30}$$

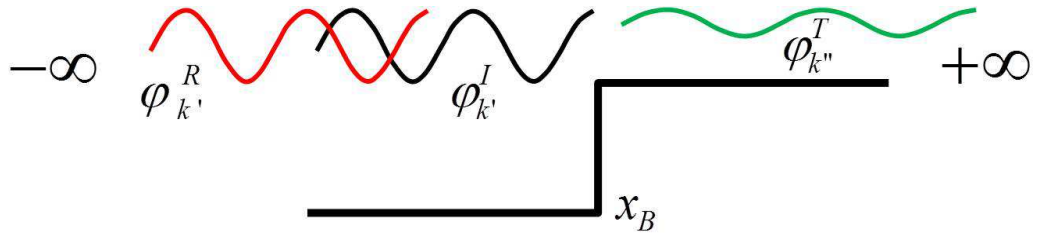

Figure 1.1: *The stationary picture of the scattering process: an incident plane waves (MWs) originated in x_0 impinging on a step V_{B}.The discontinuity x_{B} separates the scattering region, and hence the support of the solution $\psi(x,t_0)$, in two disconnected domains where the Hamiltonian of the system commutes with the momentum operator, separately. One, on the left side $\mathcal{D}_x^-$ of the barrier, contains the linear superposition of the two (incident and reflected) MWs, while the complementary $\mathcal{D}_x^+$ contains only the transmitted MW.*

which, can be viewed in the form of (1.21) if assuming the operator S has the following form:

$$S = \begin{pmatrix} t & r \\ r & t \end{pmatrix} \tag{1.31}$$

In that scheme, it is possible to calculate the relevant physical quantities. In particular, the usual relation for the transmission and reflection coefficients T and R in the case of step potential, are given by

$$\begin{aligned} T(k) &= t^2\frac{k''}{k'} = \frac{4k'k''}{(k'+k'')^2} = \frac{4\sqrt{E(k)(E(k)-V_{\mathrm{B}})}}{2E(k)-V_{\mathrm{B}}+\sqrt{E(k)(E(k)-V_{\mathrm{B}})}} \\ R(k) &= r^2 = \frac{(k'-k'')^2}{(k'+k'')^2} = \frac{2E(k)-V_{\mathrm{B}}+\sqrt{E(k)(E(k)-V_{\mathrm{B}})}}{2E(k)-V_{\mathrm{B}}-\sqrt{E(k)(E(k)-V_{\mathrm{B}})}} \end{aligned} \tag{1.32}$$

Although the standard scheme guarantees the conservation of the total flux, to deal with real cases one needs to consider the particle in terms of a wave packet. This is the goal of the next section.

1.3.3 Scattering of a Gaussian Wave Packet

Now we introduce the standard scheme for the scattering of a Gaussian wave packet, in analogy with the MWs scheme. The particle $\psi(x,t)$ is described by an incoming GWP $\Psi_{\rm in}(x,t)$ of the form (1.6), starting very far from the potential and proceeding toward the step following equations (1.14). When the GWP interacts with the potential the system enters in a transitory regime in which it starts to bifurcate in opposite directions (Fig.1.2), forming transmitted and reflected wave packet. Once the demixing is complete and the different components have completely non overlapping supports, the two out states enter in the asymptotic regime in which they are described two Gaussian, respectively $\Psi^{\rm T}_{\rm out}(x)$ and $\Psi^{\rm R}_{\rm out}(x)$, and proceed following equations (1.14).

Also in this case general solution in coordinate space can be expressed as:

$$\psi(x,t) = \begin{cases} \Psi^{\rm I}(x,t) + \Psi^{\rm R}(x,t) & \text{for} \quad x \in \mathcal{D}_x^- \\ \Psi^{\rm T}(x,t) & \text{for} \quad x \in \mathcal{D}_x^+. \end{cases} \tag{1.33}$$

where, in this case, $\psi(x,t)$ is the whole wave function at any time t.

The general solution can be written as:

$$\psi(x,t) = \left[\Psi^{\rm I}(x,t) + \Psi^{\rm R}(x,t)\right]\Theta(x_{\rm B} - x) + \Psi^{\rm T}(x,t)\Theta(x - x_{\rm B}) \tag{1.34}$$

In the asymptotic regime it holds:

$$\begin{aligned} \psi_{\rm in}(x,t) &= \Psi^{\rm I}_{\rm in}(x,t) \\ \psi_{\rm out}(x,t) &= \Psi^{\rm T}_{\rm out}(x,t) + \Psi^{\rm R}_{\rm out}(x,t) \end{aligned} \tag{1.35}$$

Consequently with the axioms of quantum mechanics, the definition of transmission T and reflections R, is basically the probability to find the

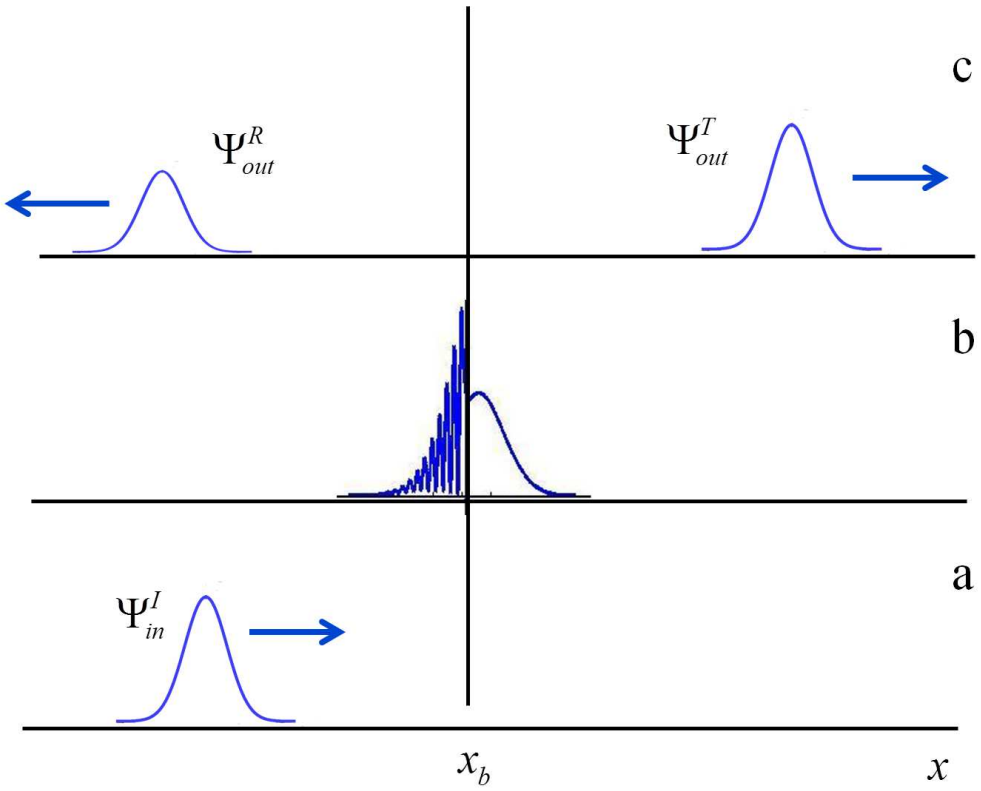

Figure 1.2: *Picture of the scattering of a GWP: the sequence of panel show the dynamics of the GWP. It starts very far from the potential and moves towards the discontinuity* x_{B}*. When interacts with the potential it bifurcates in two GWP which, once the demixing is completed, proceed in opposite directions.*

particle respectively beyond and before the discontinuity, in the asymptotic regime:

$$\begin{aligned} T &= \int |\Psi^{\mathrm{T}}_{\mathrm{out}}(x,t)|^2 \mathrm{d}x \\ R &= \int |\Psi^{\mathrm{R}}_{\mathrm{out}}(x,t)|^2 \mathrm{d}x \end{aligned} \tag{1.36}$$

and, by virtue of duality properties of momentum space, we also have:

$$\begin{aligned} T &= \int |\Phi^{\mathrm{T}}_{\mathrm{out}}(k,t)|^2 \mathrm{d}k \\ R &= \int |\Phi^{\mathrm{R}}_{\mathrm{out}}(k,t)|^2 \mathrm{d}k \end{aligned} \tag{1.37}$$

Note that the last relations implies that quantities T and R cannot depend on origin x_0 of the original incident GWP $\Phi^{\mathrm{I}}_{\mathrm{in}}(x,t_0)$.

An analytical expression for T and R can also be deduced in terms of the initial GWP $\Phi^{\mathrm{I}}_{\mathrm{in}}(k)$ and transmission $T(k)$ and reflection $R(k)$ coefficients (see (1.32)) associated to each component, given by equations:

$$\begin{aligned} T &= \int |\Phi^{\mathrm{I}}_{\mathrm{in}}(k,t_0)|^2 T(k) \mathrm{d}k \\ R &= \int |\Phi^{\mathrm{I}}_{\mathrm{in}}(k,t_0)|^2 R(k) \mathrm{d}k \end{aligned} \tag{1.38}$$

However, despite the fact that the (1.38) are widely used, to the best of our knowledge, a rigorous proof of their validity seems neglected by literature and often bypassed by the help of some approximation which invokes the sharpness of the momentum distribution of the GWP, hence bringing back to the monochromatic case.

Here we want to provide an analytical demonstration of the identities (1.38) in a very general case and for any kind of Gaussian packet. To proof

equations (1.38), we first recall the relations for transparency T and reflection R coefficients for a scattering particle on a potential step $V(x)$ in the following symmetric form:

$$V(x) = \begin{cases} V_0^- & \text{for} \quad x < 0 \\ V_0^+ & \text{for} \quad x > 0 \end{cases} \tag{1.39}$$

where $x_0 = 0$ is the scattering center and V_0^+ and V_0^- are constant values. Due to parity conservation, without loss in generality, we can assume $V_0^+ > V_0^-$.

In this contest, we consider the complete orthogonal set of stationary solutions of the Schrödinger equation:

$$\begin{aligned} \varphi_{\pm k'}(x) &= (2\pi)^{-1/2} \mathrm{e}^{i \pm kx} \\ \varphi_{\pm k''}(x) &= (2\pi)^{-1/2} \mathrm{e}^{i \pm k''x} \end{aligned} \tag{1.40}$$

where

$$\begin{aligned} k' &= \sqrt{2m(E - V^-)/\hbar^2} \quad \text{for} \quad x < 0 \\ k'' &= \sqrt{2m(E - V^+)/\hbar^2} \quad \text{for} \quad x > 0 \end{aligned} \tag{1.41}$$

Approaching the potential from the left, and recalling the general solution (1.24), the transmitted and reflected coefficients $t(k)$ and $r(k)$ are respectively can assume the following symmetric form:

$$\begin{aligned} t(k) &= \tfrac{2\sqrt{k'k''}}{k'+k''} \\ r(k) &= = \tfrac{k'-k''}{k'+k''} \end{aligned} \tag{1.42}$$

Their square modulus is interpreted as the transmission and reflection probability and obey to the conservation of the total flux:

$$|t(k)|^2 + |r(k)|^2 = 1 \tag{1.43}$$

In the Scattering matrix picture, connecting incoming and outgoing states, this leads to the following compact form for the solution with left incoming wave:

$$\psi_{\text{out}}(x) = S\psi_{\text{in}}(x) \tag{1.44}$$

where

$$\begin{aligned} \psi_{\text{in}} &= \psi_k^{\text{I}}(x) \\ \psi_{\text{out}}(x) &= \psi_k^{\text{T}}(x) + \psi_k^{\text{R}}(x) \end{aligned} \tag{1.45}$$

and the scattering operator S has the form of (1.31).

Once the connection rules for incoming and outgoing waves have been established, we now have to translate them into the non stationary framework, in terms of Gaussian wave packet (GWP). In this case we deal with asymptotic state defined in section (1.3.1): *in* (Ψ_{in}) and *out* (Ψ_{out}) *asymptotes*

Under suitable asymptotic conditions [44], orthogonality and completeness are guaranteed. It assures that if the Ψ_{in} is a GWP it evolves, after the scattering, in a Ψ_{out}, which is a GWP jet for quadratic, linear, or constant potentials only and that [14].

Also in this case the evolution of the system is obtained by the use of the S matrix, connecting *in* states with *out*, as follows:

$$\Psi_{\text{out}} = S\Psi_{\text{in}} \tag{1.46}$$

where Ψ_{in} is the asymptotic incident GWP and

$$\Psi_{\text{out}} = \Psi_{\text{out}}^{\text{T}} + \Psi_{\text{out}}^{\text{R}} \tag{1.47}$$

is the sum of the two asymptotic transmitted ($\Psi_{\text{out}}^{\text{T}}$) and reflected ($\Psi_{\text{out}}^{\text{R}}$) GWPs. Moreover, the conservation of the norm of the wave function is guaranteed by the unitary of the S matrix.

Now, to proof the relation (1.38) we must expand the above relations (1.46) on the plane waves base, noting that in the asymptotic conditions *in*

and *out* packet must be expanded in the appropriate set of planes waves:

$$\Psi^{\mathrm{T}}_{out}(x) = \int \Phi^{\mathrm{I}}_{in}(k,t_0)\varphi_{(+k'')}(x)^* S \varphi_{(+k'')}(x)\mathrm{d}k \tag{1.48}$$

Now, by the use of (1.44) we perform the operator S on the *in* waves obtaining:

$$\Psi^{\mathrm{T}}_{out}(x) = \int \Phi^{\mathrm{I}}_{in}(k,t_0)\varphi_{(+k'')}(x)^* t(k) \varphi_{(+k')}(x)\mathrm{d}k \tag{1.49}$$

Note that the same relations hold for the reflected case, simply substituting the label T by R, that is:

$$\Psi^{\mathrm{R}}_{out}(x) = \int \Phi^{\mathrm{I}}_{in}(k,t_0)\varphi_{(-k')}(x)^* r(k) \varphi_{(-k')}(x)\mathrm{d}k \tag{1.50}$$

Finally performing the norm of both side of (1.49), we obtain:

$$\begin{array}{rcl} T & = & \int |\Phi^{\mathrm{I}}_{\mathrm{in}}(k)|^2 t^2(k)\mathrm{d}k \\ R & = & \int |\Phi^{\mathrm{I}}_{\mathrm{in}}(k)|^2 r^2(k)\mathrm{d}k \end{array} \tag{1.51}$$

Recalling definitions (1.27), (1.51) are exactly the relations (1.38) required. We stress that the above procedure to deduce equations (1.51), can be performed not only in the case of step potential but for a wide class of potential, only changing the definition of the scattering matrix S adopted.

We stress that, (1.38) results as an exact formula, irrespective of any approximation on the momentum distribution of $\Phi^{\mathrm{I}}_{\mathrm{in}}(k',t_0)$

- Chapter 2 -

The Schrödinger Simulator

In this chapter we report the method used to implement our code for the numerical solution of the Schrödinger equation. A Crank-Nicholson finite difference scheme is adopted, with absorbing boundary conditions, such that no reflection emerges. The absorbing boundary conditions are used to emulate the wave packet propagation to infinity. Our code works in 3-d, with any number and shape of barriers.

§ 2.1 Finite Difference Approximation

Consider the time-dependent three dimensional Schrödinger problem in $\Omega \times [0, T]$ and in atomic units,

$$\begin{cases} i\dfrac{\partial \Psi(\mathbf{r}, t)}{\partial t} = H_t \Psi(\mathbf{r}, t) \\ \Psi(\mathbf{r}, 0) = \Psi_0(\mathbf{r}) \\ \mathbf{D}\Psi(\mathbf{r}, t)|_{\partial\Omega} = 0 \end{cases} \tag{2.1}$$

where H is the Hamiltonian (1.1) $\Omega \subseteq \Re^N$, T is the time domain $\partial\Omega$ the spatial domain boundary. Operator $\mathbf{D}$ defines the boundary condition imposed on a solution. In case of bounded and sufficiently small spatial domain $\mathbf{D}$ is the identity operator, so the boundary condition is reduced to $\Psi(\partial\Omega, t) = 0$.

To solve the problem (2.1) numerically means basically to find a solution of a discrete problem defined in the nodes of a grid covering the space-time domain, which would converge to the real solution of the initial equation in terms of some grid norm once the discretization steps are turned to zero.

Let $h_i,\ i = 1..N$ (N is the number of points)and τ be discretization steps along each spatial dimension and time axes respectively. Then we can define a lattice in space-time domain as

$$W = \left\{(x_{n_1,...,n_N}, t_m)\right\} = \left\{x_1^0 + n_1 h_1, ..., x_N^0 + n_N h_N\right\} \times$$

$$\times \left\{m\tau\right\} = W_r \times W_t, \quad n_i, m = 0, 1, 2, ... \quad i = 1..N$$

Here h_i and τ are space and time lattice steps respectively.

In Cartesian coordinates the Laplacian is written as

$$\nabla^2 = \sum_{i=1}^{N} \frac{\partial^2}{\partial x_i^2}$$

Therefore by replacing the derivatives in equation (2.1) with finite differences we obtain the standard weighted implicit-explicit scheme [17],[21]:

$$\begin{cases} i\dfrac{u^{m+1}_{n_1,...,n_N} - u^{m}_{n_1,...,n_N}}{\tau} = \\ = \theta \mathbf{H}_h^{m+1} u^{m+1}_{n_1,...,n_N} + (1-\theta) H_h^m u^m_{n_1,...,n_N} \\ u^0_{n_1,...,n_N} = \Psi_0(x_{n_1,...,n_N})\ \forall x_{n_1,...,n_N} \in W_r \\ \mathbf{D}_h u^{m+1}_{\partial\Omega} = 0 \end{cases} \tag{2.2}$$

where $u^m_{n_1,\ldots,n_N} = u(x_{n_1,\ldots,n_N}, t_m)$ is a discrete function defined on the lattice W, $u^{m+1}_{\partial\Omega}$ - function values at the domain boundary and $\mathbf{D}_h$ is the discretized boundary conditions operator. The discrete finite difference representation of a time-dependent Hamiltonian is defined as follows

$$H^m_h u^m_{n_1,\ldots,n_N} = -\frac{1}{2}\times$$
$$\sum_{i=1}^{N} \frac{u^m_{n_1,\ldots,n_i-1,\ldots,n_N} - 2u^m_{n_1,\ldots,n_i,\ldots,n_N} + u^m_{n_1,\ldots,n_i+1,\ldots,n_N}}{h_i^2} +$$
$$+V(x_{n_1,\ldots,n_i,\ldots,n_N}, t_m) u^m_{n_1,\ldots,n_i,\ldots,n_N}.$$

In order to secure convergence of the solution of the discrete problem (2.2) to the true solution of the partial differential equation (2.1) the scheme (2.2) must be consistent and numerically stable (the Lax-Richtmyer theorem) [17],[42]. The initial value problem for the partial differential equation is supposed to be well-posed here, i.e. its the solution must exist, be unique and depend continuously on the problem data (initial condition and right-hand part). The well-posedness of initial-boundary value problem for Schrödinger equation has been established (see, e.g. [20]).

Generally, the discrete scheme $\mathbf{\Lambda} u^m_n = 0$ is *consistent* [17] with the continuous problem $\mathbf{L}\Psi(x,t) = 0$ if it approximates the initial problem, i.e. the residual error at each grid point can be kept as small as desired by appropriate selection of the discretization steps:

$$\mathbf{\Lambda} u^m_n - \mathbf{\Lambda}\Psi(x_n, t_m) \sim o(\tau^p + h^q),$$

$p, q \geq 1$ - order of the approximation.

The scheme $\mathbf{\Lambda} u^m_n = 0$ is said to be stable with respect to initial data if

$$\left\|u^m\right\| \leq C\left\|u^0\right\| \quad \forall m \ , \tag{2.3}$$

where $C > 0$ is a constant which doesn't depend on discretization steps h and τ, $\|.\|$ is some grid norm on space lattice W_r [39].

There several estimations of the scheme (2.2) parameters h, τ and θ can be found in literature which guarantee the scheme stability with respect to different grid norms (see, for example, [17],[39]). However, there's a stronger condition which should be taken into account here through the physical nature of the problem: the wave function L_2-norm preservation

$$\int_\Omega \Psi(x,t)\Psi^*(x,t)dx = 1 \ \forall t$$

or, in terms of discrete functions

$$\left\|u^m\right\|_{L_2} = \left\|u^0\right\|_{L_2} = 1 \ \forall m.$$

Evidently, if the solution preserves its L_2-norm at each layer of time grid, the condition (2.3) holds true automatically ($C = 1$). To find out when this unitarity condition is satisfied, we rewrite the equation (2.2) the following way [21]:

$$u^{m+1} = \mathbf{U}(m, m+1)u^m \tag{2.4}$$

where $\mathbf{U}(m, m+1) = \left(1 + i\theta\tau\mathbf{H}_h^{m+1}\right)^{-1}\left(1 - i(1-\theta)\tau\mathbf{H}_h^m\right)$ is the system time evolution operator.

In order to preserve the L_2-norm (i.e. the scalar product in Hilbert space) $\left\|u^{m+1}\right\|_{L_2} = \left\|u^m\right\|_{L_2}$ the evolution operator must be unitary [19]. It is known that eigenvalues of a unitary operator reside on a unitary sphere. In the simplest case of time independent Hamiltonian $\mathbf{H}_h$ the eigenvalues λ_k of $\mathbf{U}(m, m+1)$ are the functions of eigenvalues of $\mathbf{H}_h$ (discrete finite set ϵ_k)

$$\lambda_k = \frac{1 - i(1-\theta)\tau\epsilon_k}{1 + i\theta\tau\epsilon_k}$$

and both operators have the same set of eigenvectors [21]. The eigenvalues norm is

$$\left|\lambda_k\right| = \left[\frac{1+(1-\theta)^2\tau^2\epsilon_k^2}{1+\theta^2\tau^2\epsilon_k^2}\right]^{1/2}.$$

It is easy to see that the solution norm preservation condition $\left|\lambda_k\right| = 1\ \forall k$ holds true only for $\theta = \frac{1}{2}$.

For time dependent potential (and, therefore, time dependent Hamiltonian) the situation is more complicated. No θ can be found such that the wave function norm keeps its unitarity with time. Nevertheless, for $\theta = \frac{1}{2}$ (Crank-Nicholson scheme) the following norm evolution expression is obtained in [21]:

$$\left\|u^{m+1}\right\| = \left(1+O(\tau^3)\right)\left\|u^m\right\|.$$

Therefore the solution norm growth can be controlled by proper time discretization step selection.

2.1.1 Absorbing Boundary Conditions

If the considered area is infinite (e.g. the interval $[0,\infty)$), the boundary condition $\Psi(\infty,t)=0$ cannot be directly implemented numerically by cutting off the right end of the interval in certain point a and setting up $\Psi(a,0)=0$ (if a is selected close to the area of our interest, the reflected waves will interfere with the real solution while choosing a too far away will yield either significant computational costs or low precision). In order to suppress the influence of spurious reflected waves the operator $\mathbf{D}$ is selected such that it "absorbs" the passing wave instead of reflecting it thus emulating the wave propagation to infinity.

Let's consider the one-dimensional plane wave $\phi(x,t) = e^{-i(\omega t - kx)}$ travelling towards the right end of 1-d domain. By substituting the plane wave

expression into equation (2.1), we will obtain the following "dispersion relation" [9]:

$$k^2 = 2(\omega - V) \tag{2.5}$$

Resolving the expression (2.5) with respect to wave number k and remembering that only solutions with positive k travel beyond the domain (if we had been considering the left end of the domain segment, we would have taken solutions with negative wave numbers only), we will get the following boundary condition

$$k = \sqrt{2(\omega - V)} \tag{2.6}$$

The problem is that we cannot express this relation in form of some differential operator in wave functions space unless it is approximated with some rational expression.

The idea introduced in [9] addresses the notion of a wave packet group velocity. Imagine we observe the wave packet travelling with the group velocity v, $v > 0$. From (2.5) we find

$$v = \frac{d\omega}{dk} = k \tag{2.7}$$

Using the correspondence between k and $-i\frac{\partial}{\partial x}$ we can write the relation (2.7) in operator form:

$$\left(i\frac{\partial}{\partial x} + v\right)\Psi = 0 \tag{2.8}$$

If the differential equation (2.8) is satisfied on the right domain boundary, then the wave packet travelling to the right with the group velocity v will be completely absorbed thus yielding no reflection off the boundary.

In case the solution is formed by several groups of waves travelling with

different group velocities v_j the condition (2.8) can be generalized as

$$\prod_{j=1}^{q}\left(i\frac{\partial}{\partial x}+v_j\right)\Psi=0 \tag{2.9}$$

Note that, for waves traveling to the left, v_j are substituted with $-v_j$.

For example, for q = 2 we observe two wave packets propagating towards the right border with group velocities v_1 and v_2 respectively. Neither of the wave packets will be reflected out of the boundary if (using again wave number k notation for the sake of convenience)

$$k^2-(v_1+v_2)k+v_1v_2=0$$

or, using dispersion relation (2.5)

$$2(\omega-V)-(v_1+v_2)k+v_1v_2=0.$$

Going back to differential form by substituting ω and k with corresponding operators $i\frac{\partial}{\partial t}$ and $-i\frac{\partial}{\partial x}$ respectively, we obtain the boundary condition at the right end of the domain which absorbs either of wave packets travelling with the group velocities v_1 and v_2:

$$ic_1\frac{\partial\Psi}{\partial t}=-i\frac{\partial\Psi}{\partial x}+\big(c_1V-c_2\big)\Psi \tag{2.10}$$

where $c_1=\dfrac{2}{v_1+v_2}$, $c_2=\dfrac{v_1v_2}{v_1+v_2}$.

For the waves travelling left with the same velocities we must change sign before each of v_j thus getting

$$ic_1\frac{\partial\Psi}{\partial t}=i\frac{\partial\Psi}{\partial x}+\big(c_1V-c_2\big)\Psi.$$

Similar considerations can be used to obtain the boundary conditions in domains of greater number of dimensions.

2.1.2 One-Dimensional Case

In case of a particle with one degree of freedom the spatial domain turns into an interval $\Omega \subseteq \Re$.

Suppose the interval is infinite. In this case we select certain boundary points such that the finite segment $\big[a, b\big]$ would cover the area of our interest and define the initial-value problem on this segment, taking the boundary conditions in form (2.10):

$$\begin{cases} i\dfrac{\partial \Psi(x,t)}{\partial t} = -\dfrac{1}{2}\dfrac{\partial^2 \Psi(x,t)}{\partial x^2} + V(x,t)\Psi(x,t) \\ \\ \Psi(x,0) = \Psi_0(x) \\ \\ ic_1 \dfrac{\partial \Psi}{\partial t}\Big|_{x=a} = \; i\dfrac{\partial \Psi}{\partial x}\Big|_{x=a} + \; \big(c_1 V(a,t) - c_2\big)\Psi \\ \\ ic_1 \dfrac{\partial \Psi}{\partial t}\Big|_{x=b} = -i\dfrac{\partial \Psi}{\partial x}\Big|_{x=b} + \; \big(c_1 V(b,t) - c_2\big)\Psi \end{cases} \tag{2.11}$$

The uniform lattice on $\big[a, b\big] \times \big[0, T\big]$ is

$$W = \big\{a = x_0, x_1, ..., x_N = b\big\} \times \big\{0 = t_0, t_1, ..., t_M = T\big\},$$
$$x_n = x_0 + nh, \; t_m = m\tau, \; h = \frac{b-a}{N}, \; \tau = \frac{T}{M}.$$

The Crank-Nicholson finite difference scheme for regular (internal) lattice points gives

$$\begin{aligned} i\frac{u_n^{m+1} - u_n^m}{\tau} = \frac{u_{n-1}^{m+1} - 2u_n^{m+1} + u_{n+1}^{m+1}}{4h^2} \; + \\ + \frac{u_{n-1}^m - 2u_n^m + u_{n+1}^m}{4h^2} + \frac{1}{2}V_n^{m+1}u_n^{m+1} \; + \frac{1}{2}V_n^m u_n^m \end{aligned} \tag{2.12}$$

The approximation error of this scheme is estimated as $O(h^2+\tau^2)$ [17],[39]. Regrouping the items in (2.12), we get the following evolution equation at

internal points

$$\begin{aligned}\frac{i}{4h^2}\,u_{n-1}^{m+1}+\left(\frac{i}{\tau}-\frac{1}{2h^2}-\frac{V_n^{m+1}}{2}\right)u_n^{m+1}\;+\\ +\frac{i}{4h^2}\,u_{n+1}^{m+1}=-\frac{i}{4h^2}\,u_{n-1}^{m}\;+\\ +\left(\frac{i}{\tau}+\frac{1}{2h^2}+\frac{V_n^{m}}{2}\right)u_n^{m}-\frac{i}{4h^2}\,u_{n+1}^{m}\;,\\ n=1..N-1\end{aligned}\tag{2.13}$$

Finite difference approximation of boundary conditions at left and right boundary, respectively

$$ic_1\frac{u_0^{m+1}-u_0^m}{\tau}=\frac{i}{2}\left(\frac{u_1^{m+1}-u_0^{m+1}}{h}+\frac{u_1^m-u_0^m}{h}\right)+$$
$$+\frac{1}{2}(c_1V_0^{m+1}-c_2)u_0^{m+1}+\frac{1}{2}(c_1V_0^m-c_2)u_0^m$$

and

$$ic_1\frac{u_N^{m+1}-u_N^m}{\tau}=-\frac{i}{2}\left(\frac{u_N^{m+1}-u_{N-1}^{m+1}}{h}+\frac{u_N^m-u_{N-1}^m}{h}\right)+$$
$$+\frac{1}{2}(c_1V_N^{m+1}-c_2)u_N^{m+1}+\frac{1}{2}(c_1V_N^m-c_2)u_N^m$$

gives the equations for u_0^{m+1} and u_N^{m+1}:

$$\begin{aligned}\left(\frac{ic_1}{\tau}+\frac{i}{2h}-\frac{c_1V_0^{m+1}-c_2}{2}\right)u_0^{m+1}-\frac{i}{2h}\,u_1^{m+1}=\\ =\left(\frac{ic_1}{\tau}-\frac{i}{2h}+\frac{c_1V_0^{m}-c_2}{2}\right)u_0^{m}+\frac{i}{2h}\,u_1^{m}\end{aligned}\tag{2.14}$$

and

$$\begin{aligned}\left(\frac{ic_1}{\tau}+\frac{i}{2h}-\frac{c_1V_N^{m+1}-c_2}{2}\right)u_N^{m+1}-\frac{i}{2h}\,u_{N-1}^{m+1}=\\ =\left(\frac{ic_1}{\tau}-\frac{i}{2h}+\frac{c_1V_N^{m}-c_2}{2}\right)u_N^{m}+\frac{i}{2h}\,u_{N-1}^{m}\;.\end{aligned}\tag{2.15}$$

Summarizing (2.13), (2.14) and (2.15), we can write a system evolution equation in a form

$$\mathbf{A}u^{m+1} = \mathbf{B}u^m$$

or

$$u^{m+1} = \mathbf{A}^{-1}\mathbf{B}u^m \tag{2.16}$$

Matrices $\mathbf{A}$ and $\mathbf{B}$ are tri-diagonal. Equation (2.16) defines the procedure of the numerical solving of the time-dependent Schrödinger equation in one-dimensional case. Therefore, unless the matrix $\mathbf{A}$ is singular, the solution of the finite difference problem exists and is uniquely defined by the initial vector u^0. Note that the system evolution operator $\mathbf{U}(m, m+1) = \mathbf{A}^{-1}\mathbf{B}$ is calculated at each time iteration, unless the potential V is time independent; in that case it is calculated just once for all the time steps.

- Chapter 3 -

Validation of the Schrödinger Simulator

In this chapter, we discuss the implementation of the physical observables to describe separately the three different components coming out the scattering process. After description of the dynamical behaviour of the numerical solution of Schrödinger equation, we provide a validation method to evaluate the quality of the description of our code and giving confidence to our results.

§ 3.1 Testing the Simulator

Figures 3.2-3.3, panels (a), show the scattering of a GWP on a potential $V_{\mathrm{B}} = 1$ a.u., with energy respectively, slightly down ($k_0 = 1.28$) and slightly up (1.54) a.u. the barrier, both of them originated at the same distance $\Delta x = x - x_0 = 30$ a.u. and with the same $\sigma_x(0) = 2$ a.u. The different curves correspond to different time steps $t_1, ..., t_6$ of the GWP evolution.

Panel (b) of Figs.3.2-3.3 shows the whole $\Psi(x,t)$ after scattering in the asymptotic regime, that in our case coincides with the stability of both $||\Psi^{\mathrm{T}}_{\mathrm{out}}(x,t)||$ and $||\Psi^{\mathrm{R}}_{\mathrm{out}}(x,t)||$ within an accuracy of 10^{-5} (see Fig.3.5), with

the same $\Delta x = 30$ a.u., while panels (c) show the asymptotic curves with the same setting as in (b) but with a larger $\Delta x = 80$ a.u.

Comparing panels (b) and (c) of both above figures at different k_0, we can figure that both the shape of asymptotic GWP's slightly differs varying their origins, while, the larger Δx the more larger oscillations of the slower tail appears.

Moreover, figures show that the centers $\langle x(t) \rangle$ of each asymptotic reflected and transmitted component are shifted along the respective directions of the motion by an amount increasing with Δx.

However, more interesting is how $\langle x(t) \rangle$ varies with Δx but for fixed k_0. Also in this case the GWP's centers are shifted forwards and hence a larger formation time is expected. This is confirmed by panels (a) of Figs. 3.2-3.3 and Fig. 3.5 where the transient regime is reported. We can recognize that both $|\Psi^{\mathrm{T}}(x,t)|^2$ and $||\Psi^{\mathrm{T}}||$, (and the same for the reflection) depend on x_0, and in particular the time interval to reach the asymptotic regime increases with Δx.

Finally, looking only at panels (b) of Figs. 3.2-3.3, we obtain a simple trend for both the components after scattering : the asymptotic $|\Psi^{\mathrm{T}}_{\mathrm{out}}(x,t)|^2$ and $|\Psi^{\mathrm{R}}_{\mathrm{out}}(x,t)|^2$ are lower and have larger width with respect to the incident $|\Psi^{\mathrm{I}}_{\mathrm{in}}(x,t)|^2$, and also their relative magnitude depends strictly on initial momentum k_0, namely $|\Psi^{\mathrm{T}}_{\mathrm{out}}(x,t)|^2$ is larger (smaller) than $|\Psi^{\mathrm{R}}_{\mathrm{out}}(x,t)|^2$ for $k_0 - k_{\mathrm{B}} > 0$ ($k_0 - k_{\mathrm{B}} < 0$).

§ 3.2 Physical Observables

Once the discrete solution of Schrödinger equationwas obtained, we deal with the implementation of most of the interesting physical operators, such as,

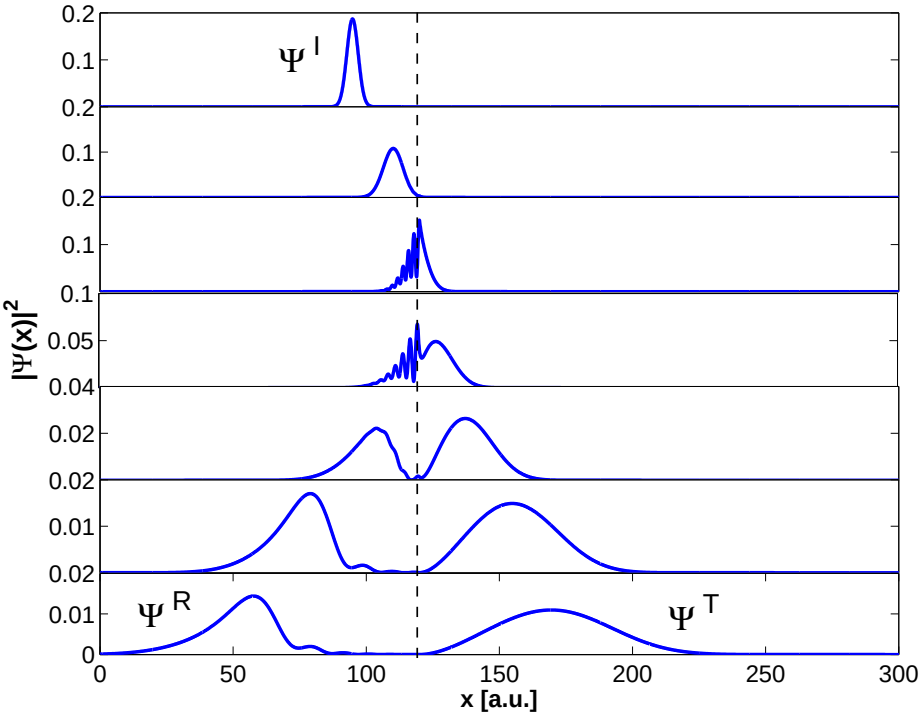

Figure 3.1: *Picture of the scattering of a GWP provided by our code, with:* $k_0 = 1.54 a.u.$, $x_{\mathrm{B}} = 120 a.u.$ *and* $V_{\mathrm{B}} = 1 a.u.$

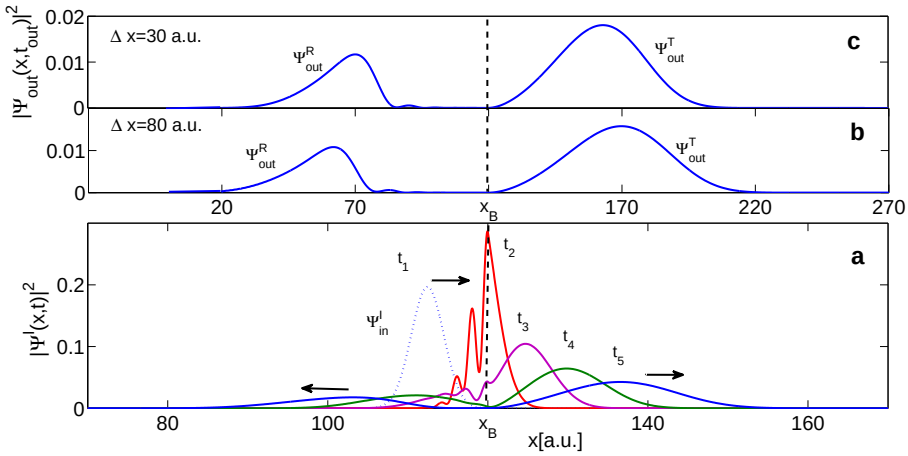

Figure 3.2: *GWP's dynamics. The* $|\Psi(x)|^2$ *with* $k_0 = 1.28$ *a.u. is reported for different increasing time steps* $t_1....t_{\rm as}$*, where* t_{as} *is the time in which the WF reach its asymptotic regime.*

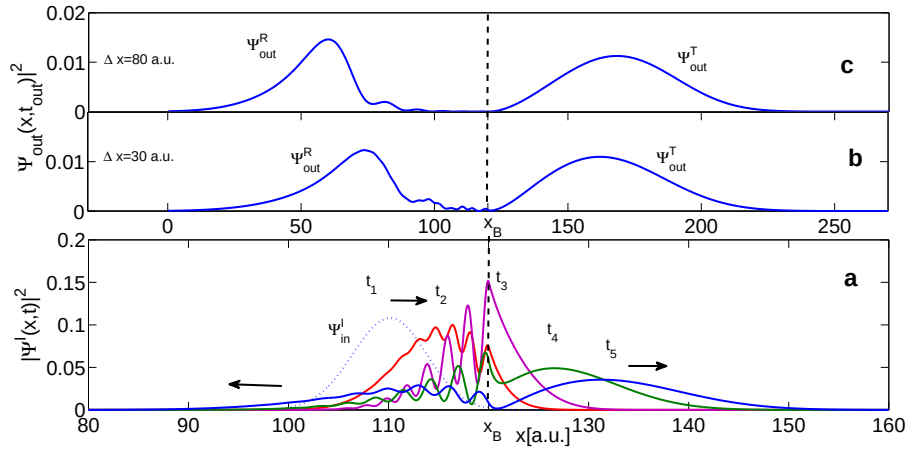

Figure 3.3: *GWP's dynamics. The norm* $|\Psi(x)|^2$ *with* $k_0 = 1.54$ *a.u. is reported for different increasing time steps* $t_1....t_{as}$*, where* $t_{\rm as}$ *is the time in which the WF reach its asymptotic regime.*

energy E, position X, momentum K, and probability of transmitted and reflected particle, T and R.

In order to manage independently the different components, outgoing the scattering, $\Psi^{\mathrm{T}}_{\mathrm{out}}(x)$ and $\Psi^{\mathrm{R}}_{\mathrm{out}}(x)$, we must first separate the whole wave function $\Psi_{\mathrm{out}}(x,t)$, and than we follow the dynamics for $t \to +\infty$ of each components, which proceed in opposite directions in coordinate space (see Fig. 3.4).

As we have seen in section 1.3.3, soon after the scattering, the system spends a certain time for completely demixing and reaching the asymptotic regime (see Fig. 3.5), in which the two components assume definitively their values $\Psi^{\mathrm{T}}_{\mathrm{out}}(x)$ and $\Psi^{\mathrm{R}}_{\mathrm{out}}(x)$. Very far from the potential their supports in coordinate space can be assumed to be not connected.

Recalling (1.33) and (1.35), we are able to obtain every components through the numerical solution u^m_n provided by our code :

$$\begin{aligned}
\Psi^{\mathrm{I}}_{\mathrm{in}}(x,t) &\equiv \left\{u^{\mathrm{I}}_{in}\right\}^m_n = u^{m<m_{in}}_{n<n_{\mathrm{B}}} \\
\Psi^{\mathrm{T}}_{\mathrm{out}}(x,t) &\equiv \left\{u^{\mathrm{T}}_{out}\right\}^m_n = u^{m>m_{out}}_{n>n_{\mathrm{B}}} \\
\Psi^{\mathrm{R}}_{\mathrm{out}}(x,t) &\equiv \left\{u^{\mathrm{R}}_{out}\right\}^m_n = u^{m>m_{out}}_{n<n_{\mathrm{B}}}
\end{aligned} \tag{3.1}$$

where m_{in} and m_{out} are respectively the time step in which the demixing process starts (when the GWP impacts the potential step) and finish (it means $u^m_{n\geq n_{\mathrm{B}}}$ and $u^m_{n\leq n_{\mathrm{B}}}$ reach their asymptotic values. In the next section we will establish an operative criterion to measure m_{in} and m_{out}.

Also we can introduce the uniform lattice $\tilde{W}$ on the dual momentum-time domain $\left[k_a, k_b\right] \times \left[0, T\right]$:

$$\begin{gathered}
\tilde{W} = \left\{k_a = p_0, p_1, ..., p_N = k_b\right\} \times \left\{0 = t_0, t_1, ..., t_M = T\right\}, \\
p_n = 0_0 + pl,\ t_m = m\tau,\ l = \frac{k_b - k_a}{N},\ \tau = \frac{T}{M}.
\end{gathered}$$

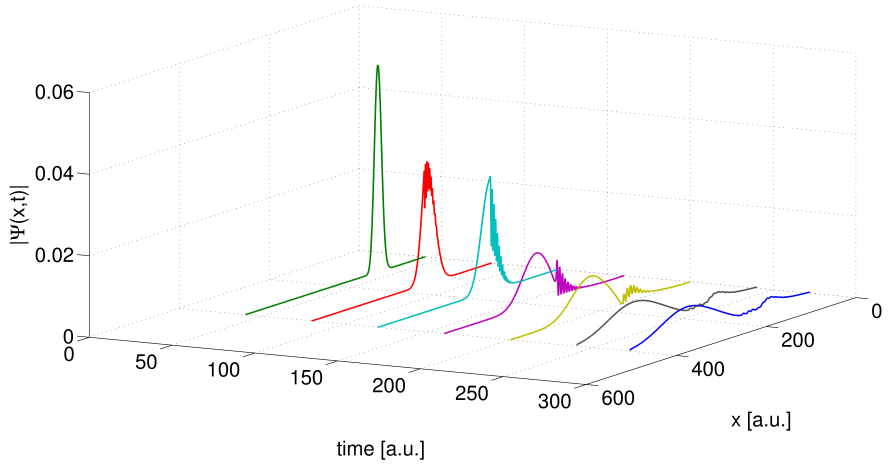

Figure 3.4: *The Scattering dynamics: an incident GWP originated in x_0 impinging on a step V_{B}, with energy slightly higher then V_{B}. When the scattering starts, the initial wave function bifurcates in opposite directions: the transmitted component, which proceeds forward and reflected component which inverts its direction.*

Performing the Fourier transformation on previous functions (3.1) we can also obtain the momentum representation of every GWPs:

$$\begin{aligned}
\Phi^{\mathrm{I}}_{\mathrm{in}}(k,t) &\equiv \left\{\tilde{u}^{\mathrm{I}}_{in}\right\}^m_p = \tilde{u}^{m<m_{in}}_{p>0} \\
\Phi^{\mathrm{T}}_{\mathrm{out}}(k,t) &\equiv \left\{\tilde{u}^{\mathrm{T}}_{out}\right\}^m_p = \tilde{u}^{m>m_{out}}_{p>0} \\
\Phi^{\mathrm{R}}_{\mathrm{out}}(k,t) &\equiv \left\{\tilde{u}^{\mathrm{R}}_{out}\right\}^m_p = \tilde{u}^{m>m_{out}}_{p<0}
\end{aligned} \tag{3.2}$$

where:

$$\begin{aligned}
\left\{\tilde{u}^{\mathrm{I}}_{\mathrm{in}}\right\}^m_p &= h\sum_{n<n_{\mathrm{B}}} e^{-ipn} u^{m<m_{in}}_{n<n_{\mathrm{B}}} \qquad p>0 \\
\left\{\tilde{u}^{\mathrm{T}}_{\mathrm{out}}\right\}^m_p &= h\sum_{n>n_{\mathrm{B}}} e^{-ipn} u^{m>m_{out}}_{n>n_{\mathrm{B}}} \qquad p>0 \\
\left\{\tilde{u}^{\mathrm{R}}_{\mathrm{out}}\right\}^m_p &= h\sum_{n<n_{\mathrm{B}}} e^{-ipn} u^{m>m_{out}}_{n<n_{\mathrm{B}}} \qquad p<0
\end{aligned} \tag{3.3}$$

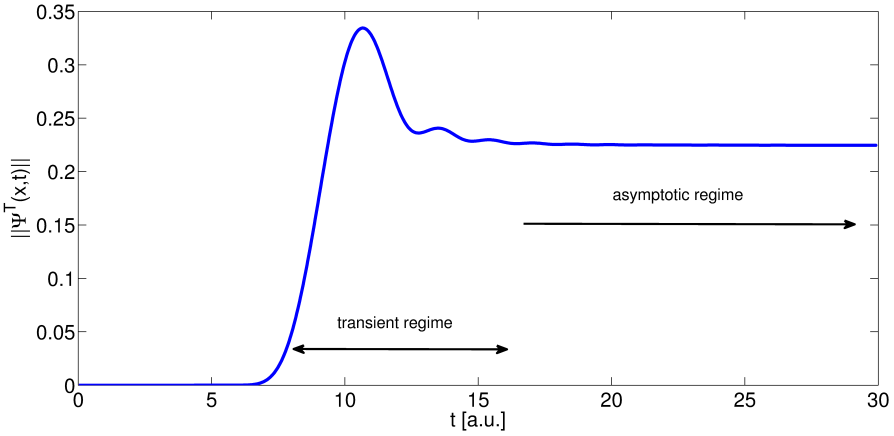

Figure 3.5: *The norm* $||\Psi^{\mathrm{T}}(x,t)||$ *of a transmitted GWP as a function of time, and with the following initial conditions:* $\Delta x = 70$ *a.u.(* $\Delta x = x_{\mathrm{B}} - x_0$ *),* $k_0 = 1.28$ *a.u.,* $\sigma_x(0) = 2$ *a.u.,* $V_{\mathrm{B}} = 1$ *a.u..*

With the above definitions we are able to compute all physical observables for each components, incident, transmitted and reflected. In particular we first calculate that quantities useful as a test to validate the code: the kinetic energy E_k, the mean value of the GWPs in coordinate and momentum space ($\langle x \rangle$ and $\langle k \rangle$), the transmission T and reflection R:

$$\begin{aligned}
\langle E_k^{\mathrm{J}} \rangle &= l \sum_p \left\{ \{\tilde{u}^{\mathrm{J}}\}_p^m \right\}^* k^2 \left\{ \tilde{u}_{in}^{\mathrm{I}} \right\}_p^m \\
\langle k^{\mathrm{J}} \rangle &= l \sum_p \left\{ \{\tilde{u}^{\mathrm{J}}\}_p^m \right\}^* k \left\{ \tilde{u}_{in}^{\mathrm{I}} \right\}_p^m \\
\langle x^{\mathrm{J}} \rangle &= h \sum_n \left\{ \{u^{\mathrm{J}}\}_n^m \right\}^* x \left\{ u_{in}^{\mathrm{J}} \right\}_n^m \\
\langle T \rangle &= l \sum_p | \left\{ \tilde{u}_{out}^{\mathrm{T}} \right\}_p^m |^2 \\
\langle R \rangle &= l \sum_p | \left\{ \tilde{u}_{out}^{\mathrm{R}} \right\}_p^m |^2
\end{aligned} \tag{3.4}$$

where, to simplify the notation, we have set $J = I, T, R$ and $\tilde{u}^{\mathrm{I}} = \tilde{u}_{in}^{\mathrm{I}}$,

$\tilde{u}^{\mathrm{T}} = \tilde{u}^{\mathrm{T}}_{out}$, and $\tilde{u}^{\mathrm{R}} = \tilde{u}^{\mathrm{R}}_{out}$.

§ 3.3 Validation of the scheme

The numerical solution of the Schrödinger equation requires the discretization (through intervals of measure h) of the space region where the phenomena are supposed to occur and of the considered time (through intervals of measure τ). Of course such need impacts on the quality of the description and is responsible for errors whose amount we need to know to give confidence to our results. Expressions 3.4, allow us to perform some validation test.

Figure 3.6 show the comparison between the mean kinetic energy (E_k) of the whole wavefunction and the sum of the transmitted mean kinetic energy (E^{T}_k) and the reflected one (E^{R}_k), as a function on time. As we can see, far before and soon after the scattering, the following relation is verified:

$$E_k = TE^{\mathrm{T}}_k + RE^{\mathrm{R}}_k \tag{3.5}$$

Figure 3.7 shows the behaviour of the momentum mean value for the whole, transmitted and reflected wavefunction as function on time. Fig.3.7 also shows the comparison between the above quantities computed trough two methods: the first one makes use of (3.4) and the second one computing the derivative of the respective mean value of position, as established by the Ehrenfest's theorem. The comparison shows that the two methods coincides for each component, at least in the asymptotic regime.

Finally we compare the transparency T computing via the two expression (1.36) and (1.37). In the following we accept $\epsilon_0 = 10^{-6}$ corresponding to the finest grid mash available for our machine. In this validation scheme we considered a GWP with $k_0 = 1.54$ a.u. and $\sigma_k = .025$ a.u. impacting a

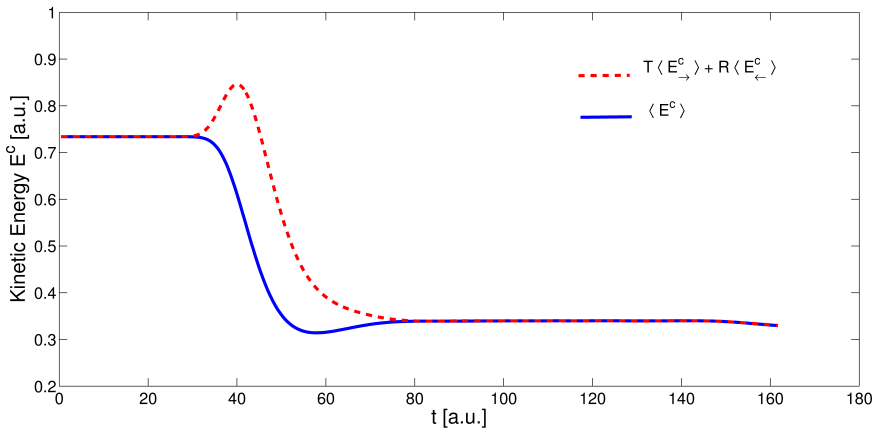

Figure 3.6: *comparison between the mean kinetic energy E_k (total wavefunction) and the weighted sum of the transmitted energy E_k^{T} and the reflected one E_k^{R}*

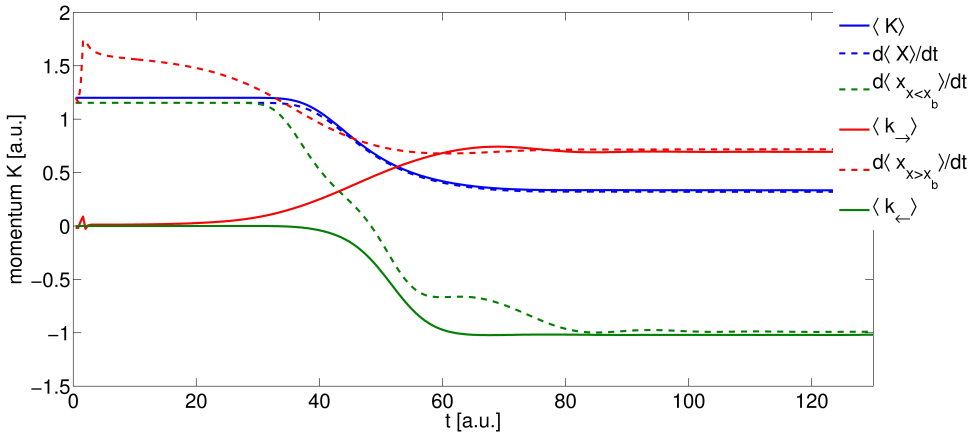

Figure 3.7: *Comparison between transmitted and reflected mean value of momentum computed using* (3.4) *and by the derivative of the mean value of position.*

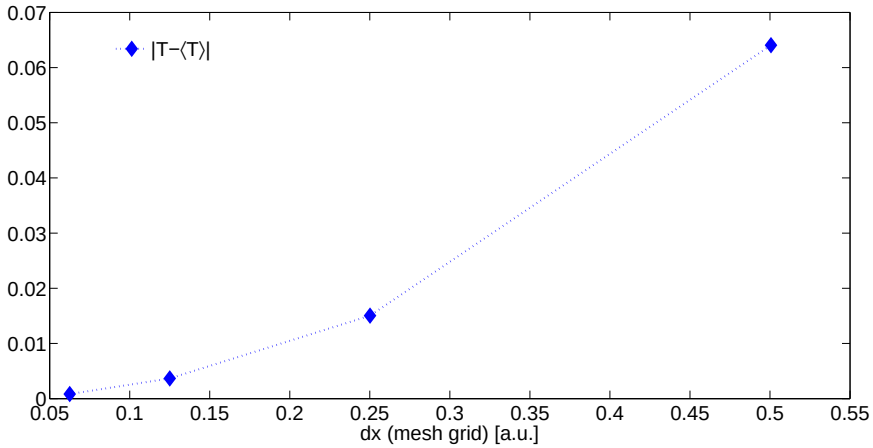

Figure 3.8: *Difference between T computed via* (1.37) *and* (1.36)*, as a function on the step h of the grid mesh*

potential well of height $V_0 = 1$ eV.

Figure 3.8 shows the difference of the two expression for T, varying with the grid mesh.

Table 3.1 shows that for the default grid mesh step the two quantities give consistent results within a confidence of 10^{-3}.

Table 3.1: *Difference between T computed via* (1.37) (1.36)*, as a function on the step h of the grid mesh.*

$10^{-3}\Delta T$	$h[a.u]$	$10^{-3}\tau[a.u]$
.8	0.062	0.166
3.6	0.125	0.333
15.4	0.250	0.666
64.5	0.500	2.001

- Chapter 4 -

Results and Discussion

In this chapter we introduce the characteristic time interval formation time (t_f) and we provide a method to quantitatively describe it. After we have showed the dependence of such a time interval , on the origin x_0 of the incident GWP we also provide a semi-classical model to describe t_f only in terms of initial conditions. A comparison with the numerical simulation is reported to sustain the model.

§ 4.1 The *formation time*

As a consequence of eq.(4.1), that here we report for convenience:

$$\begin{aligned} \overline{T} &= \int |\Phi^{\mathrm{I}}_{\mathrm{in}}(k,t_0)|^2 T(k)\mathrm{d}k \\ \overline{R} &= \int |\Phi^{\mathrm{I}}_{\mathrm{in}}(k,t_0)|^2 R(k)\mathrm{d}k \end{aligned} \tag{4.1}$$

the above T and R quantities are independent of the initial position x_0 of the incident GWP and they depend only on the initial GWP momentum

distribution, whose modulus is constant on time. Rather, an inspection of Figure 4.1 and 4.2 shows immediately that, within the confidence limits, the time spent to reach the asymptotic value $\overline{T}$ increases with the separation of the initial position from the step. The same result can be showed for the reflected probability $\overline{R}$.

Here, we will just define the time interval spent by the system to reach $\overline{T}$, which we call *formation time* t_{f}, relating it to the dynamical variables of the incident GWP.

Due to the non-compactness of the Gaussian functions, strictly, the scattering process of a GWP through a barrier starts once the GWP is present and ends in the limit of time t approaching infinity. However, the evolution of the system can be characterized by two different dynamical regimes (see Fig.3.5) introducing the approximations, clarified in the following paragraph.

Far from the potential, the front of the incident GWP weakly interacts with the barrier. For all practical purpose, the GWP moves towards the barrier as a free packet. Once the interaction between the front of the GWP and the potential become relevant, the system starts to bifurcate in opposite directions, forming transmitted and reflected wave packets (see Fig.1.2), with one or multiple peaks, as suggested in [5]. We call this time instant t_{in}. For $t > t_{\mathrm{in}}$, the system enters in a transient regime dominated by the superposition of the incoming and reflected waves, in the $x < x_{\mathrm{B}}$ zone, and by the oscillating distribution probability in the $x > x_{\mathrm{B}}$ zone. On the other hand, after the tail of the incident GWP has arrived to the barrier, oscillations decrease with increasing time and, after a sufficient long time, the transmitted and reflected probability distributions approach a limit value, corresponding to the theoretical values expressed by eqs.(1.36) (see Fig.3.5). Strictly, the demixing process is complete only in the limit of time t approaching infinity,

where the system could be considered decoupled in transmitted and reflected free packets with non-overlapping supports. However, also in this case, we can consider a finite time limit $t_{\rm out}$ such that, for $t > t_{\rm out}$, the system enters into an asymptotic regime, characterized by the two resulting GWPs escaping as free packets from the barrier and assuming definitively their constant distributions and probabilities in momentum space. Finally, we define the characteristic formation time as the interval $t_{\rm f} = t_{\rm out} - t_{\rm in}$. Let's concentrate our attention on the GWP of the transmitted particle. Determining the interval $t_{\rm f}$ requires finding the two time limits ($t_{\rm in}$, $t_{\rm out}$) of the scattering region. Within the confidence limits, they respectively represent the time step in which the front of the incident GWP impinges the potential step, yielding a non zero transmitted probability, and the time step in which the transmitted GWP approaches the $\overline{T}$ value. Thus, $t_{\rm in}$ and $t_{\rm out}$ can be operatively determined assigning a confidence accuracy $\epsilon_{\rm r}$ (hereafter we use a value $\epsilon = 10^{-2}$) while $t_{\rm f}$ can be deduced calculating the time interval spent by the norm $||\Psi^{\rm T}(x,t)||$ to pass from $\epsilon_{\rm r}$ to the value $||\Psi^{\rm T}_{\rm out}||$ - $\epsilon_{\rm r}$ (Fig. 3.5). By definitions, it follows that:

$$\begin{aligned} ||\Psi^{\rm T}(x,t_{\rm in})|| &= \epsilon_{\rm r} \\ ||\Psi^{\rm T}(x,t_{\rm out})|| &= T - \epsilon_{\rm r} \\ t_{\rm f} &= t_{\rm out} - t_{\rm in} \end{aligned} \tag{4.2}$$

In such a way we have defined the characteristic time $t_{\rm f}$ as the time required to a fixed amount (namely 0.99) of the normalized probability of the transmitted wave packet to be observed beyond the step barrier. Moreover, the $t_{\rm f}$ values are directly accessible by our simulations. From now on, we concentrate our attention on the description of the formation time in terms of the dynamical parameters of the system.

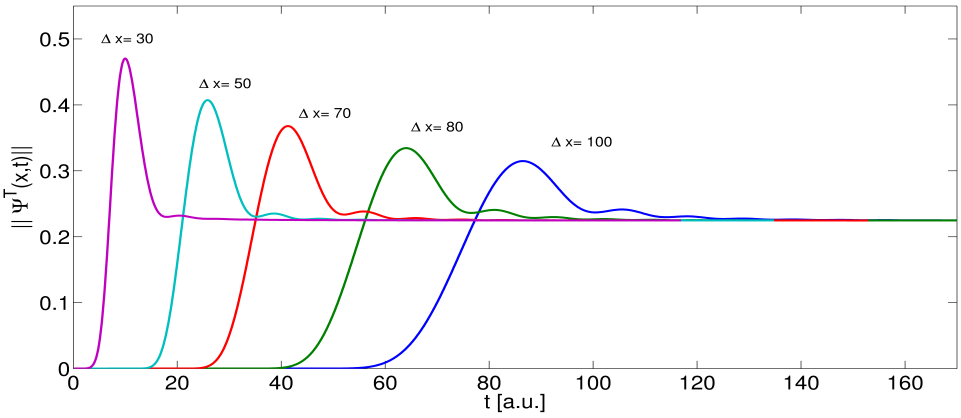

Figure 4.1: *The norm* $||\Psi^{\mathrm{T}}(x,t)||$*, with* $k_0 = 1.28$ *a.u.,* $\sigma_x(0) = 2$ *a.u., and* $V_{\mathrm{B}} = 1$ *a.u. for different initial wave packet centers* ($\Delta x = 30, 50, 70, 100$ *a.u.)*

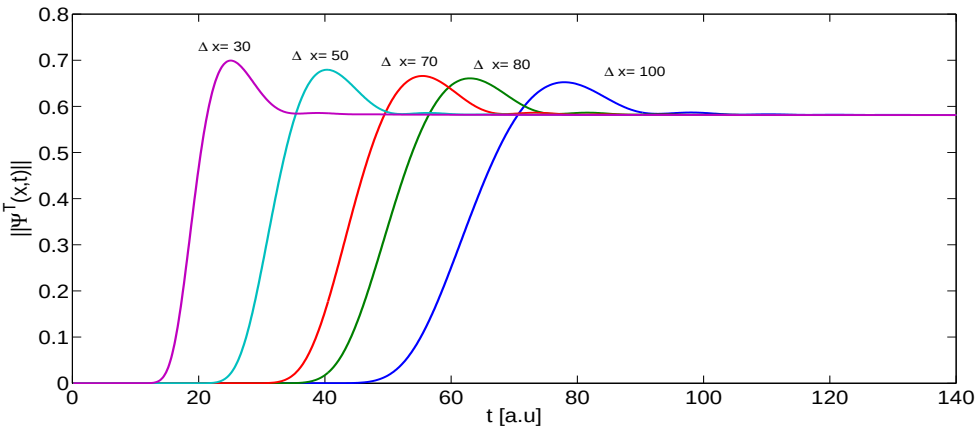

Figure 4.2: *The norm* $||\Psi^{\mathrm{T}}(x,t)||$*, with* $k_0 = 1.54$ *a.u.,* $\sigma_x(0) = 2$ *a.u., and* $V_{\mathrm{B}} = 1$ *a.u. for different initial wave packet centers* ($\Delta x = 30, 50, 70, 100$ *a.u.)*

§ 4.2 The model

In this section, we propose a model to analytically describe the formation time $t_{\rm f}$ as a function of initial conditions x_0 and $\sigma_x(0)$. First we note that $t_{\rm f}$, should be not shorter then the time required to the system to demix in two different reflected and transmitted components, even though having overlapping support. On the basis of the definitions from the previous section, this demixing process starts when the front of the incident GWP impinges the step interface and it terminates once the tail of the GWP arrives on the step. We call this time interval the *crossing time* $t_\times$. It can be seen simply as the time required to the incident GWP support to cross the coordinate $x_{\rm B}$ at the step interface. Of course, since the support of a Gaussian is not compact we must define it via some operative criterion, summarized in a parameter γ, defining the number of dispersions putatively forming the support of the GWP. To compute $t_{\rm f}$, we first consider a semi-classical model for the evolution of a free expanding GWP in the absence of the step potential $V(x)$. First, by the use of eqs.(1.14), we deduce an expression for $t_\times$ in terms of initial conditions x_0, k_0 and $\sigma_x(0)$. Then to account for the corrections, due to the interaction with the potential, we compare $t_\times$ with the real values of $t_{\rm f}$ obtained by simulations of the system in the presence of the potential $V(x)$. In this way we obtain an analytical expression explaining real $t_{\rm f}$ data, as a function of initial conditions and fitting parameters.

Consider a free GWP originated in x_0 and with momentum k_0, moving towards the coordinate position $x_{\rm B}$, first in absence of the potential $V_{\rm B}$. To calculate the time spent by the GWP to completely cross the $x_{\rm B}$ we must take into account that its motion is the combination of both the motion of its center of mass and the motion of the two fronts of the packet. Let us define

$t_{\rm a}$ and $t_{\rm b}$ respectively as the maximum time value for which the support, in coordinate space, is still totally included in the region $x < x_{\rm B}$, and at the minimum time step for which the finite support is already totally located in in the $x > x_{\rm B}$ zone, (Fig.4.3). Consistently with the definition given for $t_\times$, we obtain:

$$\begin{aligned} \langle x(t_{\rm a})\rangle &= x_{\rm B} + \gamma\sigma(t_{\rm a})/2 \\ \langle x(t_{\rm b})\rangle &= x_{\rm B} - \gamma\sigma(t_{\rm b})/2 \end{aligned} \tag{4.3}$$

Hence, $t_\times = t_{\rm b} - t_{\rm a}$. In the case of a free wave packet the relations (1.14) still hold. On the other hand, in the range of parameters in which we run, the following condition is satisfied:

$$k_0 \ll \frac{(\langle x(t)\rangle - x_0)}{2\sigma_x^2(0)} \tag{4.4}$$

which, by the use of the first of (1.14), reads:

$$\sigma_x^2(0) \ll \frac{\hbar^2 t^2}{4m^2\sigma_x^2(0)} \tag{4.5}$$

In such a regime, we can approximate the second of the equations (1.14) with the following:

$$\sigma_x(t) = \frac{\hbar t}{2m\sigma_x(0)} \tag{4.6}$$

Actually we can write an equation for $t_\times$ only in terms of initial parameters, by resolving the system composed by the first of (1.14) and (4.6) calculated in $t \equiv t_a$, and the first of (4.3). As a solution we obtain:

$$t_{\rm a} = \frac{4m\sigma_x(0)}{\hbar(4k_0\sigma_x(0) - \gamma)}(x_{\rm B} - x_0) \tag{4.7}$$

In a likely manner, by simultaneously solving the first of (1.14) and (4.6) calculated in $t \equiv t_b$, and the second of (4.3):

$$t_{\rm b} = \frac{4m\sigma_x(0)}{\hbar(4k_0\sigma_x(0) + \gamma)}(x_{\rm B} - x_0) \tag{4.8}$$

Subtracting (4.7) from (4.8), we obtain the crossing time $t_\times$ as a function of initial position x_0:

$$t_\times = \frac{8m\gamma\sigma_x(0)}{\hbar(16k_0^2\sigma_x^2(0)_0 - \gamma^2)}(x_\mathrm{B} - x_0) \tag{4.9}$$

Figure 4.4 compares t_f and $t_\times$ as a function of x_0 for different values of k_0. Both quantities show a linear dependence increasing with the separation of the origin of the incident GWP from the step.

Since $t_\times$ is the crossing time in the case of free GWP, as expected, it is settled below t_f at a fixed k_0 and the difference between $t_\times$ and t_f seems to be constant, within the confidence, also on varying k_0. Now, to get a model for t_f including the effects of the interaction, we describe the difference between the two quantities introducing a term t^*. This term takes into account the deviations from the free GWP due to the presence of the potential and we relate it to an additional dependence of the demixing process on the initial conditions x_0, k_0 and $\sigma_x(0)$, namely

$$t_\mathrm{f} \;=\; t_\times + t^* \tag{4.10}$$

A fitting procedure is required to evaluate the free parameters γ and t^*. Recalling that we supposed the origin x_0 was the leading parameters in determining t_f, through the spread $\sigma_x(t)$ in the scattering region, here we assume a linear fitting functions both for γ and t^* on x_0, with α and β as fitting parameters.

$$\begin{aligned} t^* &= t^*(x_0, \alpha, \beta) \\ \gamma &= \gamma(x_0, \alpha', \beta') \end{aligned} \tag{4.11}$$

Equations (4.10) and (4.11) define the semi-classical linear model only in terms of initial parameters and the fitting parameters α, β and α', β':

$$t_\mathrm{f} = t_\times(x_0, k_0, \sigma_x(0), \gamma(x_0, \alpha', \beta')) + t^*(x_0, \alpha, \beta) \tag{4.12}$$

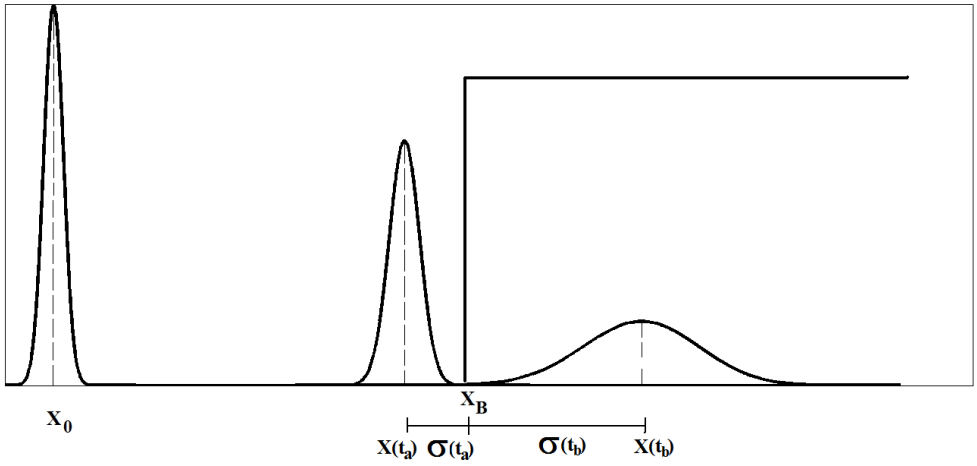

Figure 4.3: *Evolution of a GWP, originally centered in x_0, passing from incoming time t_a to outgoing time t_b*

After performing a set of simulations to evaluate t_f, through the definition (4.2), we compare the results with data provided by the model (4.12). For initial values x_0, k_0 and $\sigma_x(0)$ in the range considered, we obtain the values $\alpha = -2.422$, $\beta = 411.632$ and $\alpha' = -0.004$, $\beta' = 19.895$, as fitting parameters. Figure 4.5 plots both simulated and expected t_f values, as a function on x_0 and at different k_0 and with fixed $\sigma_x(0) = 2$ a.u. Actually, the formation time given in eq.(4.12) results to be different from t_f in eq.(4.2): this could be ascribed to the influence of the initial conditions on wave packets with large momentum spread [30] The value of γ seems to depend slightly on x_0, and it is appreciably different from the free values ($\gamma = 6\sigma_x(0)$). This is due to the variations caused by the presence of the potential.

The above equations establish a connection between t_f and initial parameters of the system. Results show a relevant dependence of the dynamics of the wave packet on the origin x_0. In particular t_f, i.e. the interval time needed to make accessible the outgoing wave packets for experimental measurements, is

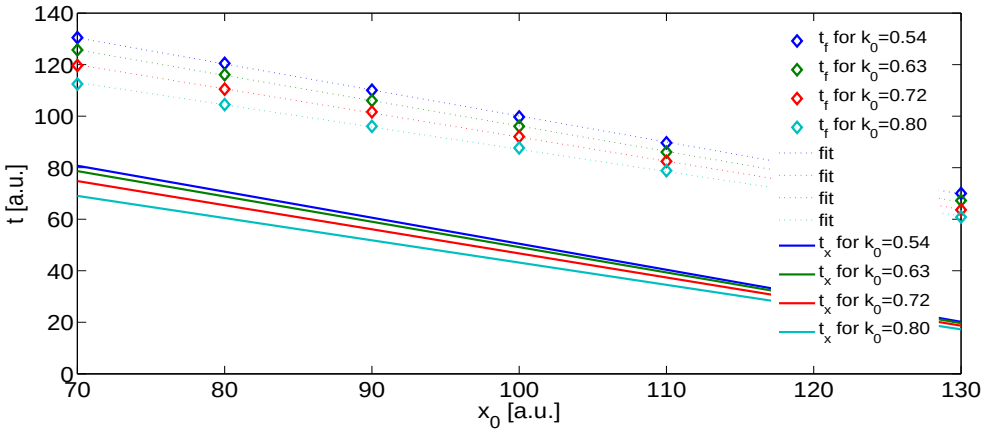

Figure 4.4: *Comparison between* t_{f} *and* $t_{\times}$ *as a function of* x_0 *for initial values* $k_0 = 0.54, 0.63, 0.72, 0.80$ *a.u.,*$V_{\mathrm{B}} = 0.2$ *a.u. and* $x_{\mathrm{B}} = 150$ *a.u. is The family of diamonds are the data from simulations by the use of* (4.2)*; dotted lines are the correspondent regression curves; the full lines are the data obtained by* (4.9).

strongly dependent on the origin and increases with the separation from the barrier ($\Delta x = x_{\mathrm{B}} - x_0$). At the same time, due to the norm conservation, the maximum value of the probability density, as a function on time, decreases with x_0.

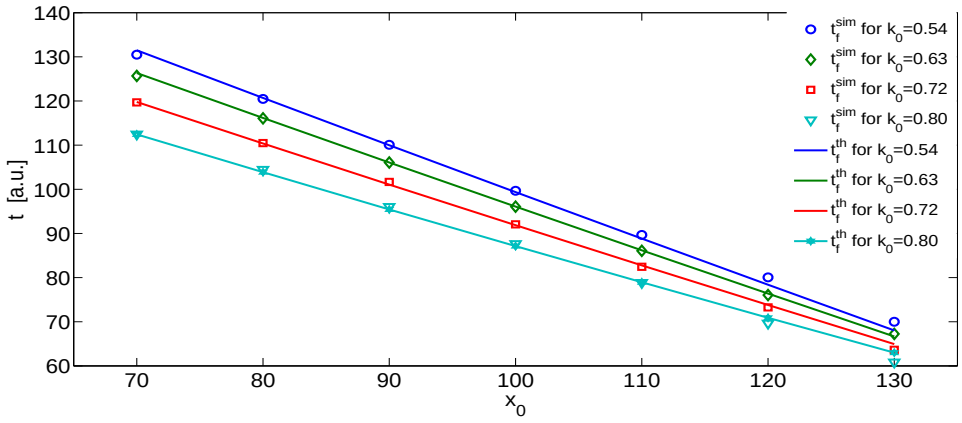

Figure 4.5: *Comparison between* t_{f}*, as a function of* x_0 *for initial values* $k_0 = 0.54, 0.63, 0.72, 0.80$ *a.u.,* $V_{\mathrm{B}} = 0.2$ *a.u. and* $x_{\mathrm{B}} = 150$ *a.u, obtained by the use of* (4.2) *(diamonds) and by* (4.11) *(full lines).*

Conclusions

Usually, mainly for practical purposes, the description of the scattering event is provided in terms of monochromatic waves instead of a wave packet, relaxing the description assuming that the particle energy E is well defined around its mean value. There are however a number of situations that are characterized by the fact that the incoming particles are generated at a finite distance from randomly distributed scattering centres and with an energy spread that is comparable to the potential height, so they cannot be reduced to a monochromatic waves scheme. In this scenario, the initial conditions x_0 and $\sigma_x(0)$ can assume a relevant role in the description of the dynamics of the system. However describing the system in terms of Gaussian wave packet requires resolving numerically the Schrödinger equation. Hence, through the numerical solution, we analyse the evolution of the Gaussian wave packet, calculating the transmission of the scattering Gaussian wave packet as a function of x_0, $\sigma_x(0)$ and k_0,and comparing simulated data with theoretical results. We introduce a time interval, which we call formation time t_f, as the time required to a fixed amount (0.99) of the normalized probability of the transmitted wave packet to reach the asymptotic regime after scattering. A numerical analysis of the probability of the system to cross the barrier as a function of t shows that the the formation time t_f strongly depends on the

GWP x_0 and increases with the separation from the barrier. At the same time, due to the norm conservation, the charge density decreases with x_0. In the range of parameters studied, data suggest a linear behaviour of t_f on x_0, supporting the comparison with the model (4.9) proposed for a free Gaussian. To study such dependence we propose a semi-analytical model for t_f decomposing it in two terms, linearly dependent on x_0: one describing the transit of a free GWP across the discontinuity point at the step, and the other one, describing the residual dependence both on x_0 and k_0 and explaining the deviation from linearity due to the interaction with the barrier. Results show a good match between simulations and data coming from the model, confirming it could be considered a useful tool to obtain informations on the time required to observe the particle beyond the step, at least in the range of initial parameters typically adopted in condensed matter. Such a dependence of the charge density on the coordinate x_0 could be an important issue in those system in which scattering event occur within the nanoscopic scale and the conduction mechanism of the scattered particles involves charge interactions with instabilities usually lying at the barrier interface.

List of Figures in Part II

List of Tables in Part II

Bibliography

[1] Argaman N. and Makov G., Amer. J. Phys. **68**, (2000) 69.

[2] Bohm D., *Quantum Theory* , Dover, New York (1979). 61, 70

[3] Cohen-Tannoudji C., Diu B., Laloe F., *Quantum Mechanics*, Vol.1, Wiley, (1991). 70

[4] Collins S., Lowe D. and Barker J. R., J. Phys. C **20**, (1989) 6233.

[5] De Leo S., Rotelli P. P., Physics Letters A **342**, (2005) 294–298.

100

[6] Dubois E. and Larrieu G., J. Appl. Phys. **96**, (2004) 729-737.

[7] Enders A. and Nimtz G., Phys. Rev. B, **47**, (1993) 9605. 57

[8] Escott C. C., Zwanenburg F. A. and Morello A., Nanotechnology **21**, (2010) 274018. 57

[9] Fevens T. and Jiang H., J. Sci. Comput. **21**, (1999) 255-282. 84

[10] Flügge S., *Practical Quantum Mechanics* , Vol.1, Springer–Verlag, Berlin (1994). 61

[11] Fowler R. H. and Nordheim L., "Electron Emission in Intense Electric Fields", Proceedings of the Royal Society of London, Series A, 119, (1928) 173-181. 62

[12] Fyodorov Y.V. and Sommers H.J., J. Math. Phys., **38**, (1996) 1918-1981. 57

[13] Garriz A. E., Sztrajman A., and Mitnik D., Eur. J. Phys. **31**, (2010) 785-799.

[14] Huber D. and Heller E. J., J. Chem. Phys. **87**, (1987) 5302. 63, 77

[15] Hauge E. H., Falck J. P., Phys. Rev. B, **36**, (1987) 4206. 57, 64

[16] Hauge E.H., Støvneng J. A., Review of Modern Physics **61**, 4, (1989) 917-936. 57, 64

[17] Kalitkin N.N., *Numerical Methods*, Nauka, Moscow (1978). 80, 81, 82, 86

[18] Kedzierski J., Xuan P., Anderson E. H., Bokor J., King T.-J., and Hu C., IEDM Tech. Dig., (2000) 57-60.

[19] Kolmogorov A.N. and Fomin S.V., *Elements of the Theory of Functions and Functional Analysis*, Nauka, Moscow, (1976). 82

[20] Kriess H.O., Lorenz J., *Initial-Boundary Value Problems and the Navier-Stokes Equations*, Academic Press, Boston, (1989). 81

[21] Kvaal S., *A Critical Study of the Finite Difference and Finite Element Methods for the Time Dependent Schrödinger Equation*, PhD thesis, Dept. of Physics, University of Oslo, (2004). 80, 82, 83

[22] Landau L. D. and Lifshitz E. M., *Quantum Mechanics, Non Relativistic Theory* Pergamon Press, Oxford, (1965). 61

[23] Landauer R. and Martin Th., Rev. Mod. Phys. **66**, (1994) 217-228. 57, 64

[24] Lansbergen G.P., Rahman R., Wellard C.J., Woo I., Caro J., Collaert N., Biesemans S., Gerhard Klimeck, Hollenberg LC L., and Rogge S., Nature Physics **4**, (2008) 656-661. 57

[25] Leti G., et al., Appl. Phys. Lett., **99**, (2011) 242102. 57

[26] Messiah A., *Quantum Mechanics*, Wiley, New York (1996). 61, 70

[27] Matsumoto S., Nishisaka M., and Asano T., Jpn. J. Appl. Phys., **43**, (2004) 2170-2175.

[28] Olkhovsky V. S. and Recami E., Physics Reports, **214**, 6, (1992) 339-357. 57

[29] Olkhovsky V. S., Recami R., Raciti F. and Zaichenko A. K., J. Phys. I, **5** (1995) 1351.

[30] Olkhovsky V.S., Petrillo V., Zaichenko A.K., Phys.Rev. A, **70**, 1, (2004) 034103-1-4. 106

[31] Pelster R., Gasparian V., and Nimtz G., Phys. Rev. E, **55**, (1997) 7645-7655. 57

[32] Piron C., *Mécanique Quantique. Bases et Applications* (Presses Polytéchnique Universitaires Romands, (1990).

[33] Prati E., J. Nanosc. and Nanotech., **11**, (2011) 8522-8526. 57

[34] Prati E., Hori M., Guagliardo F., Ferrari G., and Shinada T., Nature Nano., **7**,(2011) 443-447. 57

[35] Privitera G., Recami E., Salesi G., Olkhovsky V.S., Riv.Nuovo Cim. **26**, (2004) 4. 57

[36] Rosenthal E., Segev B., Phys. Rev. A, **65**, (2002) 032110. 57, 64

[37] Ranfagni A., Fabeni P., Pazzi G.P., and Mugnai D., Phys. Rev. E, **48**, (1993) 1453. 57

[38] Saltzer M., Ancherold J., Phys. Rev. A **68**, (2003) 042108.

[39] Samarskii A.A., *Introduction to the Theory of Difference Schemes*, Nauka, Moscow, (1971). 82, 86

[40] Schwabl S., *Quantum Mechanics*, (1990) 2nd edition Springer–Verlag, Berlin. 61

[41] Steinberg A.M., Kwiat P.G. and Chiao R.Y., Phys. Rev. Lett., **71**, (1993) 708. 57

[42] Strikwerda J.C., *Finite Difference Schemes and Partial Differential Equations*, Wadsworth & Brooks Cole, Pacific Grove, (1989). 81

[43] Takagi S., Toriumi A., IEEE Transactions on Electron Devices **42**, (1995) 2125-2130.

[44] Taylor J.R., *Scattering Theory: The Quantum Theory of Non relativistic Collisions*, J. Wiley & Sons, New York (1972). 67, 77

[45] Tsu R., and Esaki L., Applied Physics Letters **22**, (1973) 562-564.

[46] Tsui B. Y. and Lin C. P. , IEEE Electron Device Lett. **25**, (2004) 430-432.

[47] Tung R. T. , Phys. Rev. B, **45**, (1992) 13509-13523.

[48] Wang J., Lundstrom M., "Does source-to-drain tunneling limit the ultimate scaling of MOSFETs?" Electron Devices Meeting, (2002).

[49] Wang Z. S., Kwek L. C., Lai C. H., and Oh C. H., Phys. Rev. A **69**, (2004) 052108. 57, 64

[50] Wang Yun-ping and Zhang Dian-lin, Phys. Rev. A, **52**, (1995) 2597-2600. 57

[51] White R.L., *Basic Quantum Mechanics*, Mc Graw Hill (1966). 61, 70

[52] Yamada N., Phys. Rev. Lett., **93**, (2004) 170401. 57, 64

[53] Yeo Y.-C., King T.-J., and Chenming H., IEEE Transactions on Electron Devices, **50**, (2003) 1027.

[54] Zener C., "A Theory of the Electrical Breakdown of Solid Dielectrics". Proceedings of the Royal Society of London. Series A, **145**, (1934) 523-529.